Tectonophysics
June 2016, Volume 683, Pages 286-307
http://archimer.ifremer.fr/doc/00335/44634/

Monte Carlo approach to assess the uncertainty of wide-angle layered models: Application to the Santos Basin, Brazil

Loureiro Afonso [1, 2, *], Afilhado Alexandra [1, 3], Matias Luis [1, 2], Moulin Maryline [4], Aslanian Daniel [4]

[1] IDL - Instituto Geofísico Dom Luis, Faculdade de Ciências da Universidade de Lisboa, Edifício C8, Piso 3, Sala 8.3.31A Campo Grande 1749-016 Lisboa, Portugal
[2] FCUL - Faculdade de Ciências da Universidade de Lisboa, Portugal
[3] ISEL - Instituto Superior de Engenharia de Lisboa, Instituto Politécnico de Lisboa, Portugal
[4] Ifremer, REM-GM-LGS, F29280-Plouzané, France

* Corresponding author : Afonso Loureiro, email address : afonsoloureiro@afonsoloureiro.net

Abstract :

In the Santos Basin (Brazil), two parallel wide-angle refraction profiles show different crustal structures. One shows moderate crustal velocity gradient, and a clear Moho with topography. The other has an anomalous velocity zone, and no clear Moho reflections. This has large implications on the geological and geodynamical interpretation of the basin. Model uncertainties must be excluded as a source of these differences.

We developed VMONTECARLO, a tool to assess model uncertainty of layered velocity models using aMonte Carlo approach and simultaneous parameter perturbation using all picked refracted and reflected arrivals. It gives insights into the acceptable geological interpretations allowed by data and model uncertainty through velocity-depth plots that provide: a) the velocity-depth profile range that is consistent with the travel times; b)) the random model that provides the best fit, keeping most of the observations covered by ray-tracing; c) insight into valid models dispersion; d) main model features unequivocally required by the travel times, e.g., first-order versus second-order discontinuities, and velocity gradient magnitudes; e) parameter value probability distribution histograms.

VMONTECARLO is seamlessly integrated into a RAYINVR-basedmodelling work flow, and can be used to assess final models or sound the solution space for alternate models, and is also capable of evaluating forward models without the need for inversion, thus avoiding local minima that may trap the inversion algorithms and providing information for models still not well-parametrized.

Results for the Brazilian models show that the imaged structures are indeed geologically different and are not due to different interpretations of the same features within the model uncertainty bounds. These differences highlight the strong heterogeneity of the crust in the middle of the Santos Basin, where the rift is supposed to have failed.

Highlights

► We propose a new method to evaluate layered velocity model uncertainty. ► The method is unbiased and based on Monte Carlo simulations. ► It integrates directly on common modelling forward work-flows at any modelling stage. ► It provides uncertainty estimates without inversion. ► We show that there are different lower crustal structures in the Santos Basin profiles.

Keywords : Brazil, Santos Basin, Velocity and depth uncertainty, wide-angle seismic reflection and refraction, ray-tracing and travel time inversion, Monte Carlo; model assessment and probability distribution

1. Introduction

The Santos Basin-São Paulo Plateau System (Brazil) represents a kinematic buffer between the Central Segment and the Austral Segment of the South Atlantic Ocean (Moulin et al., 2010, 2012), and is situated immediately north of the Florianópolis Fracture Zone, one of the fundamental structures in the South Atlantic development. During the SanBa experiment, seven wide-angle refraction profiles were shot (Klingelhöfer et al., 2014; Evain et al., 2015), with the goal of better understanding the Santos-Namibe conjugate margins. Two of them were very long and parallel, crossing the Santos Basin perpendicularly to the coast (Figure 1a). The nature of the deep central Santos Basin is the key to the history of this system.

Although these parallel profiles are less than a hundred kilometres apart, their central sections have very different crustal and upper mantle structures. A parallelogram-shaped pronounced gravimetric anomaly is also evident in this region (Figure 1a), and is regarded by some authors as a tip of a propagator, but its nature is still unknown (Evain et al., 2015).

On SB01 (Figures 1b and 1e), below a 3–5 km thick, high-velocity (6.0 to 6.5 km/s), upper basement layer, there is a second 6.5 km thick layer with velocities increasing from 7.0 to 7.8 km/s from top to bottom. There are no identifiable reflection arrivals from the Mohorovičić discontinuity, but we must keep in mind that the absence of evidence does not mean the evidence of absence. The transition from the lower crust to the upper mantle was constrained by refracted arrivals and amplitude modelling (Evain et al., 2015). By contrast, on SB02 (Figures 1c and 1d), the Moho, well constrained by reflection arrivals, rises to a minimum depth of 14.5 km, but the crustal structure and velocities remain similar to those modelled on each side of this bulge, with upper (5.6 to 6.3 km/s) and lower (6.5 to 7.1 km/s) layers between 7 and 10 km thick.

The anomalous velocity structure found on SB01 (Figure 1e) is interpreted as atypical oceanic crust, exhumed lower continental crust, or intruded upper continental crust, overlying either altered mantle in the first two cases or intruded lower continental crust in the last case. The same section on SB02 (Figure 1d) is interpreted as extremely thinned continental crust (Evain et al., 2015).

When interpreting these modelling results, the main question that arises is if the different structures shown by the wide-angle models are useful for lithological interpretation or are they a consequence of the intrinsic uncertainty of the velocity models. Are the crust and Moho differently structured in the Santos Basin in such a short distance? Does the absence of clear reflections from the Moho affect the uncertainty bounds of the models?

To answer these questions, a closer look at model uncertainties was needed and we developed a new method to assess them. It is clear that the estimation of the uncertainties of the modelled

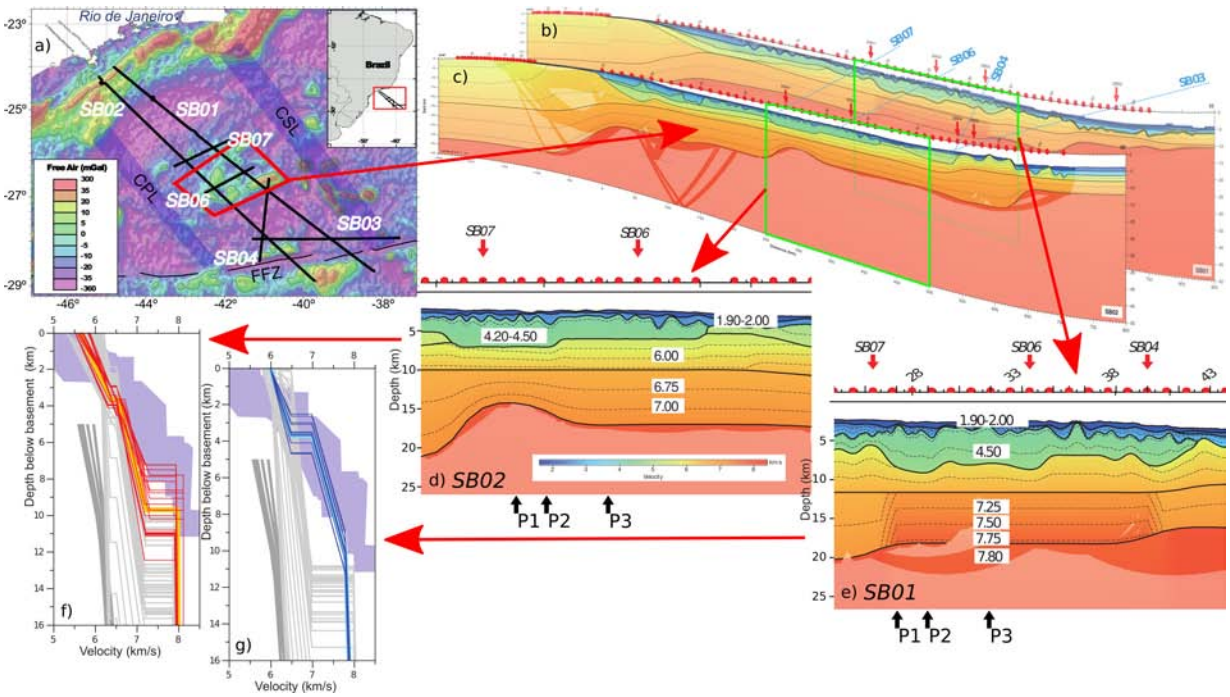

Figure 1: *a*) Gravimetric anomalies chart (Sandwell et al., 2014), with red box indicating a parallelogram-shaped high. CPL Capricórnio Lineament. CSL Cruzeiro do Sul Lineament. FFZ Florianópolis Fault Zone. Final velocity models for *b*) SB01 *c*) SB02, based on the modelling of wide-angle seismic data, adapted from Evain et al. (2015). Velocities are contoured at 0.25 km/s intervals, and black lines mark layer boundaries from the modelling. Shaded areas are unconstrained by seismic rays. Red dots mark OBS and land station positions, and arrows indicate crossings with other SanBa profiles. Dotted cyan lines indicate the positions of crossing profiles. Green vertical boxes indicate studied areas; *d*) and *e*) Zooms of studied areas of SB02 and SB01. Small black vertical arrows and P1, P2 and P3 mark locations of 1D depth-profiles used to compare the uncertainties of both profiles. *f*) and *g*) Thin blue and red lines mark 1D velocity-depth profiles extracted at 10 km interval along areas of interest of SB02 and SB01, thicker yellow and cyan line indicate mean velocity profiles. The blue shaded area bounds a compilation of velocity profiles for the Atlantic oceanic crust (White et al., 1992), and grey profiles correspond to the average velocity profiles of the five tectonic provinces defined by Christensen & Mooney (1995) plus their reference profile for continental crust.

layer velocities and interface depths is fundamental to establish the meaningful level of detail of their geological interpretation, namely concerning the lithology and geometry of the imaged structures. A velocity model interpretation should be based not only on the model itself but also on its uncertainties.

To be genuinely useful, any modelling procedure should provide *a*) a model parametrisation; *b*) error estimates on the parameters; *c*) and a statistical measure of goodness-of-fit (Press, 2007). We add that providing a measure of the uncertainty would also increase a model's usefulness.

A good knowledge of model uncertainty bounds is also fundamental when performing kinematic reconstructions, as the correct identification of the nature of structures, their spatial limits and possible mass exchanges has direct implications on the imposed reconstruction constraints (Aslanian & Moulin, 2012).

We developed VMONTECARLO, a robust algorithm to perform direct RAYINVR (Zelt & Ellis, 1988; Zelt & Smith, 1992) layered-model assessment using a Monte Carlo approach to explore an infinite solution space of a problem with under and over-determined regions. Monte Carlo methods have the advantage of allowing us to find Earth models without any bias from operator preference,

data quality or previous assumptions on geology (Press, 1968), apart from those already included in the model's parametrisation. VMONTECARLO is a tool that provides not only a measure of model uncertainty but also an insight into probable alternate solutions. These alternative solutions are extremely helpful to further understand the implications of model quality in the geological interpretation. It explores the solution space around a preferred model in order to directly assess its uncertainty, irrespective of modelling approaches, and it is capable of providing meaningful results even for models derived exclusively from forward modelling methods or where models are derived by successive forward and inverse procedures. We propose a new and simple method to evaluate the uncertainty of this latter type of seismic velocity models.

VMONTECARLO was tested with synthetic data and applied to the central sections of profiles SB01 and SB02, where an accurate geological interpretation depends greatly on the uncertainty assessment of the velocity model. Model uncertainty is directly related to lithology, homogeneity, layering and acoustic impedance contrasts inside the medium.

2. Method

2.1. Model parametrisation

Seismic imaging techniques have finite resolutions in the temporal, spatial and frequency domains. The resulting data may be corrupted by ambient noise, and is best described as inaccurate, insufficient and inconsistent (Jackson, 1972), limiting the amount of retrievable information. Any given parametrisation will be based on the limits of our imaging capabilities (Gallardo & Meju, 2011). A common approach is to parametrise a seismic velocity model as a layered medium with velocity gradients, which reflects the layered structure that is found in well samples and sonic logs. One may argue that the medium itself is continuous and it is our discrete sampling that introduces the layering, but it seems evident that no extra information is gained if we parametrise a model outside of the imaging system's resolution limits. It is also true that we can establish different, seemingly unrelated, parametrisations capable of explaining the same observations (Wigner, 1960), and we must be aware that modelling a velocity field is not the same as modelling all the physical properties of the medium.

Wide-angle seismic data modelling is often performed with the RAYINVR package (Zelt & Smith, 1992), based on trial-and-error forward modelling, seismic travel time inversion, or both. RAYINVR uses a parametrisation with interfaces and velocity gradients, allowing the interpretation and modelling of first and secondary arrivals, and several reflected and refracted phases. RAYINVR includes secondary arrivals in the modelling process, which is advantageous in some situations (Delescluse et al., 2015), chiefly when target structures are not sufficiently covered by primary arrivals. The

coarse parametrisation limits the number of free parameters (Clark et al., 2013) and, consequentially, the model space to explore. Furthermore, because the solution space for any given single type of dataset is very large, to reduce the degree of under-determination of the problem, RAYINVR allows the inclusion of additional data sources into the work-flow, such as multi-channel reflection seismics and amplitude data. It also works well with sparse instrument deployments, common in offshore profiles.

RAYINVR provides parameter uncertainty, resolution and model non-uniqueness estimates when data is inverted (Zelt & Smith, 1992), and is capable of dealing with uncommon low-velocity structures (Eccles et al., 2009) such as evaporitic deposits and sub-basalts layers. Rays are traced through the velocity model using zero-order asymptotic ray theory (Zelt & Smith, 1992; Cervený et al., 1977), which, for modelling purposes, has advantages over finite-differences methods in very complex media, because the discontinuous nature (or piecewise continuous) of the Earth is difficult to reconstruct with a fixed regular discretisation.

Current methods to assess the quality, accuracy, and precision of RAYINVR wide-angle models can be divided into indirect and direct methods (Zelt, 1999). Indirect model evaluation is often presented, usually based on the diagonal elements of the resolution matrix (for example, Sato et al., 2006), or by inclusion of a measure of smearing (Afilhado et al., 2008), linked to the off-diagonal elements of the resolution matrix. The graphical representation of velocity models usually excludes model uncertainties, but has sought to include ray coverage, reflecting interfaces and poorly-constrained sections, or interfaces without any clear reflected arrivals due to velocity inversions or unfavourable acquisition geometries (e.g. Holbrook et al., 1996). Model uncertainties can also be estimated by direct model assessment tools (Zelt, 1999), which are usually time consuming, because they expand the single parameter test to groups of parameters, and are therefore difficult to implement for all inverted parameters. Nevertheless a few examples can be found for subsets of parameter models (Holbrook et al., 1994; Viejo & Clowes, 2003; Leinweber et al., 2013). An alternative approach, that associates multi-parameter uncertainty estimate with a Markov chain Monte Carlo inversion scheme, has been proposed by Mosegaard & Tarantola (1995), and applied by Clark et al. (2013) with the implementation of Hauser et al. (2011). Uncertainties associated with different modelling approaches were also studied by Majdański (2013).

2.2. Model quality, reliability and parametrisation suitability

The quality of a model can be defined as the accuracy with which it represents the geophysical and geological observations. It depends of many factors, including the input data uncertainty and the spatial resolution the data set allows. The former sets limits to the accuracy of the modelled structures

in terms of depths and velocities, and the latter determines the minimum size of the resolvable structures, and consequently, the ability of a model to predict all the observations, meaning that in presence of small scale heterogeneities, the model may fail to properly fit all the travel times, or even fail to trace rays for some of the observables. Model roughness, or the number of parameters that define the minimum structure capable of correctly fitting the data within the estimated picking errors, is also important and, although some techniques are available to estimate the minimum structure discernible over the noise (McCaughey & Singh, 1997), the number of parameters that satisfy that condition is itself an unknown parameter, making this a trans-dimensional problem (Sambridge et al., 2006).

No generic parametrisation can provide a description of the true Earth with the best accuracy everywhere, since any approach is a gross simplification of the problem, either by using layers and gradients, or velocity grids. The best model parametrization, or the more accurate one, for each study depends on the geological target and available seismic dataset, in close relation to survey geometry, seismic instrument quality and resolution power. Although model's accuracy is hard (or even impossible) to quantify, its precision gives straight information on its quality.

The suitability of a model parametrisation is directly linked to model roughness and estimated data error levels, as it measures the adequacy of the parametrisation to the available data. An extremely under-parametrised model fails to explain data within a reasonable error, but an over-parametrised model can also mask interpretation deficiencies with the dilution of errors (Zelt & Smith, 1992). Even in models with similar parametrisations, small changes to node placement can lead to very different results. If parametrisation suitability was possible to quantify, a full error propagation analysis would provide a more reliable measure of model uncertainty.

Reliability of a model, or the robustness of the solution, measures the confidence we have on the model quality to represent the observations. Often, wide-angle work-flows are based exclusively on travel times modelling, modelling only the kinematics of seismic energy propagation. Although model quality can be established, further amplitude modelling would increase the constraints imposed on the final solution, as they account for the dynamics of the problem. The overall reliability of the model is improved if both kinematics and dynamics are adequately modelled.

2.3. Model acceptance criteria

To compare solutions, model quality must be objectively determined to accept or reject a model based on the accuracy of the predictions of the observations it is capable of. As in the present method only travel times are explored from the data set, we define criteria based on travel times fit and the number of rays the model is capable of tracing.

Travel time fit is measured by the root mean square (RMS) of the difference between the calculated and observed travel times. During modelling, a decrease of the RMS is expected, up to a value similar to the mean uncertainty of the picked travel times, without losing the ability to trace rays to a large majority of observations. At that stage, the model is considered to provide an appropriate fit to the data, since it is able to predict the observed travel times within their expected uncertainty. In this condition, the goodness-of-fit χ^2 test will produce a value of 1, indicating that data is fitted to the estimated uncertainty. Because different models are able trace rays for different data sub-sets, it is necessary to normalise the goodness-of-fit test to the number of traced rays (Zelt, 1999). Therefore, a model acceptance criteria must meet two conditions: *a*) the model is required to fit the data with an RMS similar to the data uncertainty. In other words, χ^2 is close to one; *b*) the model must be able to trace rays for at least a predefined number of observations.

2.4. Random models universe

The random models universe (RMU) defines the limits of the explorable model space for the Monte Carlo generator. It is the set of models that have the same parametrisation as the preferred model and parameter values varied within user-defined bounds.

Any model in the RMU is a permutation of all the values that the studied parameters can assume (Equations 1 and 2). In a general case, the RMU is boundless and parameters can assume any value, creating an infinite explorable model space. However, the limits for parameter variation depend on physical constraints, such as propagation velocities and depths within known limits, but mostly from the uncertainty with which data allows to determine each parameter. If the observables impose certain constraints to a parameter, they also reduce the size of the RMU.

$$P_k := \{p_k \in \mathbb{R} : p_{k_{Lower}} \leq p_k \leq p_{k_{Upper}}\} \tag{1}$$

The set P_k is the set of all the admissible values for parameter p_k, which lie between the defined lower and upper bounds $p_{k_{Lower}}$ and $p_{k_{Upper}}$. Because the values in P_k depend directly of the model acceptance criteria conditions, their range can be regarded as a priori uncertainties.

If all parameters of interest p_k are taken into account, the Random Model Universe (RMU) is a set constructed by the union of all P_k subsets, as defined by Equation 1.

$$RMU := \bigcup_{k=1}^{n} P_k \tag{2}$$

The format for the velocity files described by Zelt & Ellis (1988) and Zelt & Smith (1992) allows reducing the number of parameters for second order discontinuities across layers, fixing gradients and

layer thicknesses. If these constraints need to be studied, the omitted parameters should be inserted by hand as needed.

This study does not test the parametrisation, and assumes that sufficient care has been given to this subject. VMONTECARLO does not test if the number of parameters is adequate to correctly predict the observations or reproduce the earth's structure to any given level of detail, nor does it test if parameters are defined at the most appropriate locations. We propose an estimate of the precision of model parameter values.

VMONTECARLO builds the RMU for the given parametrisation. Testing additional parametrisations would imply creating additional RMUs, which would quickly make the problem grow to an unmanageable size.

A priori parameter uncertainties p_k can be computed using established methods, such as single parameter uncertainty estimation (Zelt, 1999), or, if other information is available, educated guesses. The latter approach is also useful in cases where ray coverage is far from optimal and calculated uncertainties are deemed too conservative.

2.5. Random model generation and scoring

If the number of parameters to test is low, a systematic exploration of the model space would be appropriate, but for the most general cases, the dimensionality of the problem remakes it computationally unfeasible (Mosegaard & Tarantola, 1995). Within the RMU, VMONTECARLO generates a large number of models $M^{(i)}$ by varying all studied parameter values $p_k^{(i)}$ independently and uniformly (Equation 3). A model $M^{(i)}$ belongs to the explorable model space only if it belongs to the RMU, which is the same as to say that all the varied parameter of interest $p_k^{(i)}$ have values in their respective subsets $P_k^{(i)}$.

$$M^{(i)} \in RMU \quad \text{if} \quad p_k^{(i)} \in P_k^{(i)} \tag{3}$$

Each of these random models is then evaluated by its ability to trace rays and fit the observations in terms of χ^2, by means of a scoring function.

To this subset of validated models from the RMU we call the Models Ensemble (ME).

$$ME := \bigcup M^{(i)} \tag{4}$$

The ME is the set of all generated models $M^{(i)}$ capable of tracing rays to the observation locations. By definition, $M^{(0)}$ is the preferred model.

In order to set up a quantitative comparison of the stochastic models, we express the ability of each model to predict the observations as a bespoke function that scores the number of traced rays, and travel time fit — the two model acceptance criteria defined in section 2.3. These quantities compare adequately the random models, as a greater number of traced rays means that a model explains a greater number of observed events, and a good statistical fit means that the errors are within the expected data uncertainty.

A good scoring function must return comparable scores for different models and data sets; whereas each data set has a different number of events and incertitudes, it must be based on normalised variables. In this case, the normalised χ^2 test value and the ratio of the number of traced rays to the number of observations are the most adequate factors, as these two parameters are easily comparable between different models.

Given these constrains, we define a suitable scoring function from the product of the ratio of predicted (*np*) and observed data (*nr*), and a lognormal distribution based on the quality of fit, with a probability density function (*pdf*) of a variable x lognormal distributed with mean μ and standard deviation σ (Equation 5).

$$pdf(x) = \frac{e^{-(ln(x)-\mu)^2/2\sigma^2}}{x\,\sigma\,\sqrt{2\pi}} \tag{5}$$

The median and standard deviation relate to the scale and shape parameters of the distribution (Croarkin & Tobias, 2012), and defines as well $x = e^{\mu-\sigma^2}$, the point where the maximum probability density is reached. For our purpose, the *pdf* is required to reach the maxima at $x = 1$, therefore we set $\mu = \sigma^2$ in (Equation 5) and obtain the *pdf* of a distribution with mean equal to variance. We then normalise this expression to obtain a function *npdf* that assumes values between zero and one (Equation 6).

$$npdf(\chi^2) = \frac{e^{-\frac{(ln(\chi^2)-\sigma^2)^2}{2\sigma^2}}}{\chi^2 e^{-\frac{\sigma^2}{2}}} \tag{6}$$

chi^2 can be regarded as lognormal distributed as it is always positive, has a sharp decay towards zero, and is calculated from several independent parameters. Using the lognormal distribution allows us to equally penalize both under and over adjusted models. To make the scoring function more or less sensitive to model quality changes, we regard the standard deviation parameter σ as a shape factor that controls the flatness of response to χ^2 value changes. To avoid confusion with the standard deviation, we call it ψ.

The scoring function $f(nr,\chi^2)$ is obtained by multiplication of this *normalised lognormal density* (Equation 6), dependent of the quality of fit (χ^2), with the ratio of predicted and observed data (Equation 7).

$$f(nr,\chi^2) = \frac{nr}{np}\frac{e^{-\frac{(ln(\chi^2)-\psi^2)^2}{2\psi^2}}}{\chi^2 e^{-\frac{\psi^2}{2}}} \tag{7}$$

Scoring function f is a function of nr, the number of traced rays, and χ^2. Response to variations of the ratio of the number of traced rays to the number of observations is linear, but response to quality of fit follows a lognormal distribution with a shape factor ψ.

The behaviour of the scoring function with the variation of both χ^2 and ψ values is shown in Figure 2. On this figure, the ratio of traced rays is kept constant $\frac{nr}{np} = 1$.

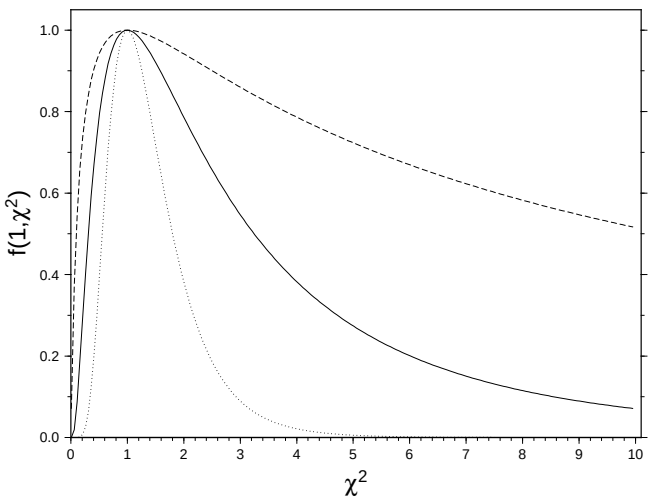

Figure 2: Scoring function $f(1,\chi^2)$ response to normalised χ^2 test values variations when $\frac{nr}{np} = 1$, with three different shape factor values: continuous line $\psi = 1$, dashed line $\psi = 2$, dotted line $\psi = 0.5$.

Number of picks, np, and the shape factor ψ are constants during each run of VMONTECARLO. The shape factor allows us to control the response of the scoring function to χ^2 variations, with higher ψ values decreasing its sensitivity. A shape factor of one is adequate for most situations. It can be changed if the distribution of scores is either unable to distinguish good from bad models or is too restrictive when accepting good models.

This scoring function has several important features: *a*) it reaches a maximum for χ^2 equal to one, decreasing monotonously to zero as χ^2 tends to infinity or zero; *b*) it gives equal scores to similar over and under misfits, i.e., $\chi^2 = 2$ and $\chi^2 = 0.5$ are equally penalised; *c*) it encompasses a shape factor to increase or reduce the sensitivity to χ^2 variations for χ^2 values close to 1; *d*) the scoring function increases monotonously with the proportion of traced rays to the total number of observations, reaching a maxima when rays are traced to all observations, and zero when no rays are traced; *e*) its codomain is limited to the interval [0, 1].

2.6. Distribution of scores plots

As it is impossible to plot scores as 2D sections in the physical space for a large ME, VMONTECARLO outputs two different graph types representing velocity-depth profiles extracted from each model, coloured according to the normalised average or maximum model scores in the ME (Figure 3b and Figure 4), and plotted over a grid using the line drawing algorithm by Bresenham (1965). This approach allows to quickly grasp the variations of interface depths and velocity gradients, as well as score distribution.

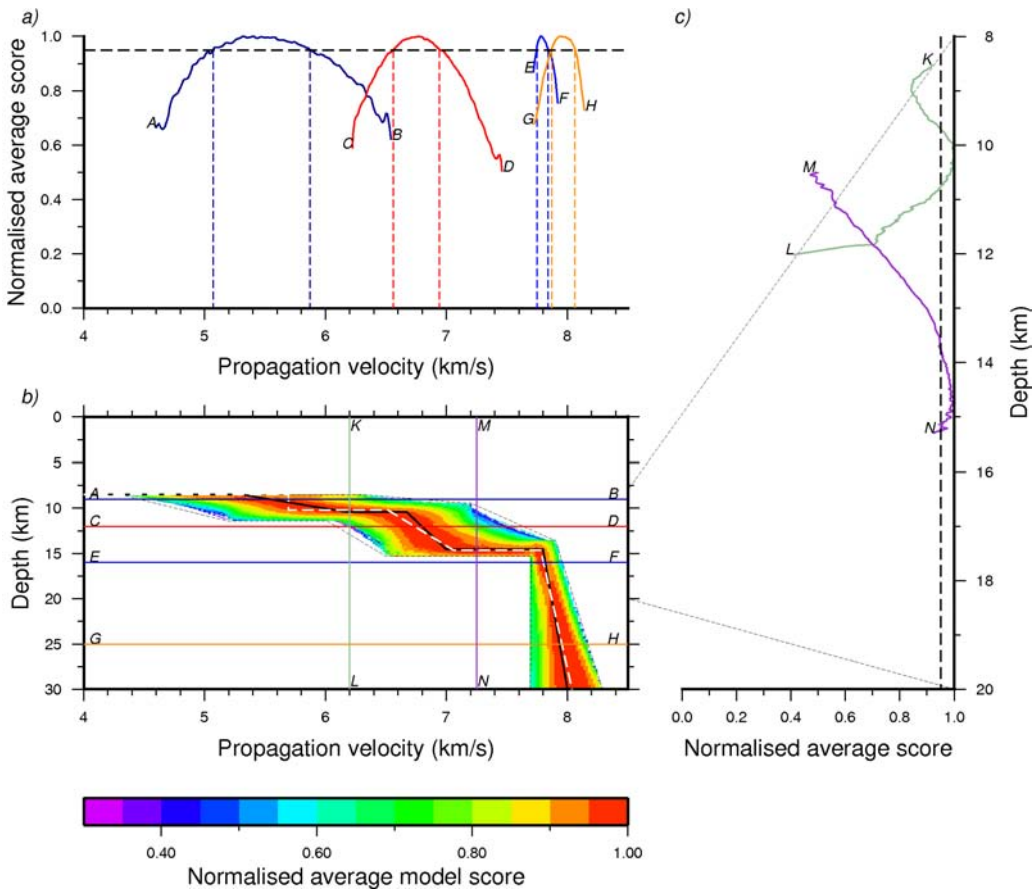

Figure 3: Normalised average models scores distribution at 240 km model distance of the entire dataset. *b*) Normalised average models scores distribution. Thin dashed lines mark independent parameter uncertainties. Solid black line indicates tested model. Dashed white line indicates best random model. Letters *A* to *H*, and *K* to *N* mark the location of the horizontal and vertical cross-sections of the average scores distribution shown in *a*) and *c*). *a*) Cross-sections of normalised average scores distribution at different depths, highlighting layer velocity gradients, with colours and letters matching the horizontal lines in *b*). Black horizontal dashed line indicates 95% of the maximum normalised average score, corresponding to the score of a model capable of tracing 95% of the original number of rays and with an increase of 3% of the original χ^2. Vertical dashed lines indicate the uncertainties at this level for the corresponding colours. *c*) Cross-sections of average scores distribution at different velocities, highlighting interface depths, with colours and letters matching the vertical lines in *b*); vertical dashed black line indicates 95% of the maximum normalised average score. The score scale is not comparable to the maximum scores figure (Figure 4), as it is not normalised.

In very complex models, plotting the same graphs using only the subset of models that comply with a definable quality threshold might be useful to highlight the skewness of the uncertainties in heterogeneous regions.

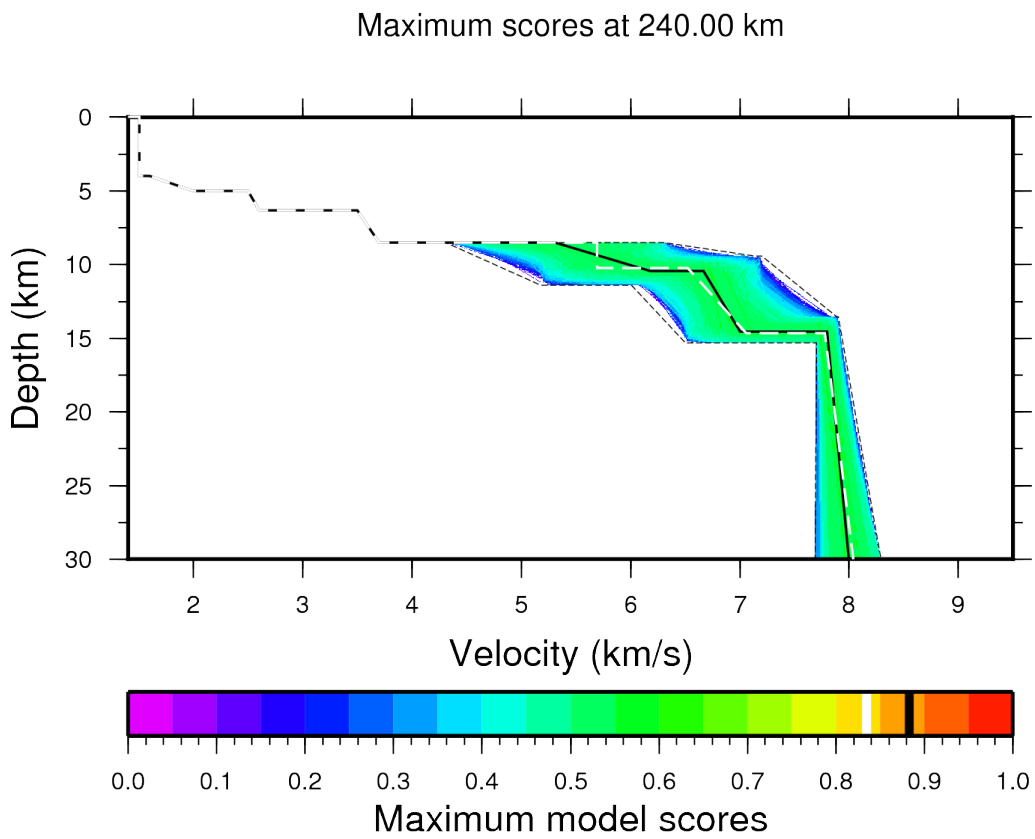

Figure 4: Maximum model scores distribution at 240 km model distance of the entire dataset. Black solid line indicates tested model. Thin dashed lines mark RMU bounds. White marker on scale indicates score of best random model. Black marker on scale indicates score of tested model. Score scale is not comparable to the normalised average scores (Figure 3), as maximum scores are not normalised.

The average scores are calculated with Equation 8, where i and j are the pixel coordinates, $f^k_{i,j}$ is the model score of the kth velocity-depth profile that crosses pixel i, j, and $C_{i,j}$ is the number of velocity profiles that cross pixel i, j. Equation 9 normalises the average scores on each velocity-depth profile by dividing each pixel value by the maximum average score value. This is done independently for each velocity-depth profile along the model.

$$\gamma(i, j) = \sum_k \frac{f^k_{i,j}}{C_{i,j}} \tag{8}$$

Function $\gamma(i, j)$ calculates the average score at each pixel (Figure 3b).

$$\Gamma(i, j) = \frac{\gamma(i, j)}{max(\gamma(i, j))} \tag{9}$$

Function $\Gamma(i, j)$ calculates the normalised average score at each pixel.

2.7. *Work-flow*

VMONTECARLO performs direct model assessment and estimates parameter uncertainties by means of a Monte Carlo simulation. In addition, the probability distribution of the velocity is com-

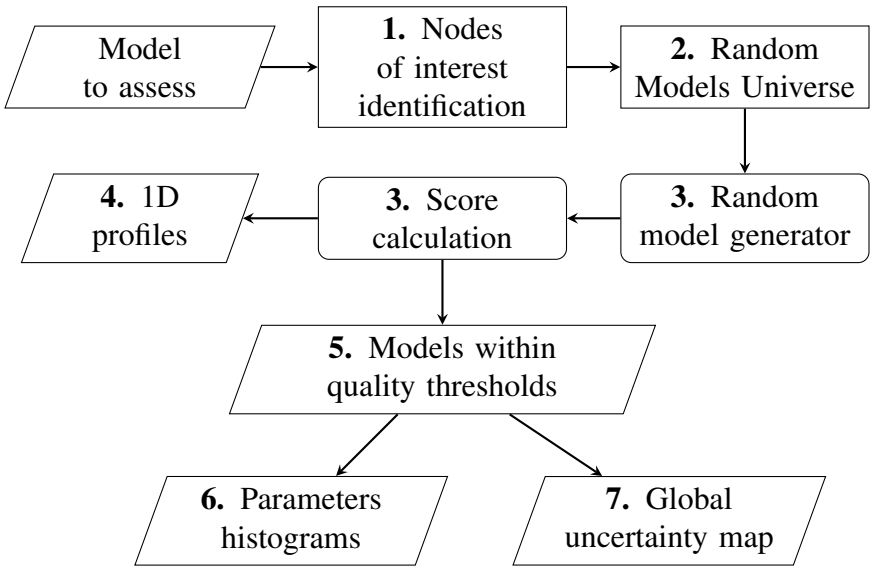

Figure 5: Flowchart for VMONTECARLO. The preferred velocity model (top left) is parsed and parameters of interest identified (1.). Maximum and minimum allowable values for each parameter define a Random Models Universe (2.). Random models are generated and scored (3.). 1D velocity-depth profiles are extracted (4.) for each model. Models within defined quality thresholds (5.) and histograms (6.) are output. Models from (5.) are used to calculate a global uncertainty map (7.).

puted anywhere in the model. This method is suitable for both forward and inverse modelling strategies at either final or intermediate stages, to evaluate a model or explore the solution space and provide alternative valid models.

The method is illustrated in Figure 5 and can be summarised as follows:

1. The velocity model file is parsed and parameters of interest are identified;
2. Maximum and minimum values for the selected model parameters are established to bound the explorable model space;
3. Within the bounds defined in (2.), the main module generates and evaluates a large number of random models, using a scoring function that measures the ability of the model to fit the data set from the ray-tracing response;
4. 1D velocity-depth profiles are extracted at chosen locations from every random model, and coloured according to the average and normalised maximum scores of the generated models;
5. A subset of models within certain quality thresholds is output;
6. For each parameter of interest, the probability distribution of the values is calculated and presented as an histogram;
7. The subset of models from (5.) is used to calculate model uncertainties and to extract a global map of uncertainties.

This method is based on travel times of direct, reflected, and turning waves, zero-offset reflections, multiples and conversions, evaluating quality of fit between predicted and observed travel times at

all stages. It does not take into account any amplitude data. Model parametrisation suitability is not evaluated, as it is expected that models are properly parametrised, in accordance with the data. Similarly, major velocity-depth trade-off issues are expected to be addressed during the modelling stage, and proper phase to interface identification is assumed. Unchanged model, observations and parameter files from the RAYINVR package are used, to provide a simple integration of the method into a typical modelling work-flow.

Users are encouraged to change and improve the code. The source code, examples, technical description and manual are available as an electronic supplement or downloadable at http://vmontecarlo.afonsoloureiro.net.

3. Application to synthetic data

To illustrate the application of VMONTECARLO, we present one example (Figure 6) of an oceanic basin model with a two layers crust with variable thickness, lateral velocity variations and top of basement topography.

We generated synthetic travel time arrivals for diving and reflected waves from the *true model* with uncertainties of 50 ms, simulating a typical acquisition geometry, with shots every kilometre and ocean-bottom seismometers every 15 km along a 300 km profile distance. Gaussian noise within 50 ms was added to the observations, but no random static shift to each OBS was applied.

To simulate the modelling work-flow, we create a *starting model* with the same parametrisation as the *true model*, but different parameter values. The travel times picks are iteratively inverted on the *starting model* until the data fit no longer improves (Table 1). After three iterations, the model fits the data with a χ^2 of 1.538, which is considered to be a fair fit. The calculated score for this model is of 0.882, using the previously defined scoring function (Equation 7) and a ψ factor equal to 1.

Iteration no.	No. of picks	No. of rays	a priori RMS (s)	RMS (s)	χ^2	Score	ψ
0	17467	16450	0.050	0.594	45.888	0.001	1
1	17467	16620	0.050	0.126	2.784	0.563	1
2	17467	16895	0.050	0.067	1.542	0.881	1
3	17467	16908	0.050	0.066	1.538	0.882	1

Table 1: Iterative inversion steps results for the synthetic example.

As generally sedimentary layers are better constrained with multi-channel reflection seismics, we apply VMONTECARLO only to the crust and upper mantle. The synthetic model has 23 parameters to test (step 1, from Figure 5), 8 upper velocity nodes, 7 base velocity nodes, and 8 depth nodes in the crust and mantle layers. Although sedimentary layers are excluded from this uncertainty evaluation, it is important to have the right geometry of the basement, because a wrong geometry would particularly

affect the ray tracing. It should also be noted that a complex basement geometry increases the non-linearity of the problem.

3.1. Random models universe

Setting the RMU is equivalent to defining boundaries for each parameter (step 2, from Figure 5). We used the results from the single parameter uncertainty test proposed by Zelt (1999) to establish these bounds. The single parameter test uses an F-test (as defined by Zelt (1999)) to indicate, with 95% of confidence, when the models are statistically different from the tested model when varying the number of data points and fit. We used this as a guide to establish the rejection thresholds for RMS, χ^2 and number of traced rays, and concluded that, without reducing the number of traced rays, the χ^2 value can be increased up to 3% and the model remains statistically the same, at a 95% confidence level.

In our implementation of the single parameter test we used four thresholds – the original F-test result, and the relative variations of RMS, χ^2 and number of traced rays. This was done to better understand how fit was affected by the different perturbation values.

The maximum perturbation values tested were of ±1.00 km (or ±1.00 km/s), as these values are expected to encompass the maximum foreseeable uncertainties of interface depths and velocity gradients for a typical model. If higher uncertainties are suspected for a given parameter, larger values should be tested.

To avoid rejecting border solutions and generate more data, we set thresholds of 10% increase in RMS or χ^2 value, and 95% of traced rays in addition to the F-test result. This means that, when compared to the original model's 16908 traced rays, χ^2 of 1.538 and RMS of 0.066 s (Table 1), models capable of tracing 16062 or more rays, with RMS under 0.073 s, a χ^2 value below 1.691 and still compliant to the F-test are accepted.

Depth parameters		
Node	**Uncertainties (km)**	
7	-1.00	1.00
8	-0.65	0.60
9	-0.50	0.55
10	-0.90	0.75
16	-1.00	1.00
17	-0.70	0.65
18	-0.90	0.55
19	-1.00	1.00

Top velocity parameters		
Node	**Uncertainties (km/s)**	
1	-1.00	1.00
2	-0.80	0.95
3	-0.85	1.00
4	-1.00	1.00
11	-0.55	0.55
12	-0.40	0.25
20	-0.10	0.10
21	-0.10	0.10

Base velocity parameters		
Node	**Uncertainties (km/s)**	
5	-1.00	1.00
6	-1.00	0.85
13	-1.00	0.85
14	-0.35	0.35
15	-0.35	0.60
22	-0.30	0.25
23	-0.30	0.30

Table 2: Estimated uncertainties for depth, top velocity and base velocity nodes for the tested model. Node numbers correspond to the ones in Figure 6

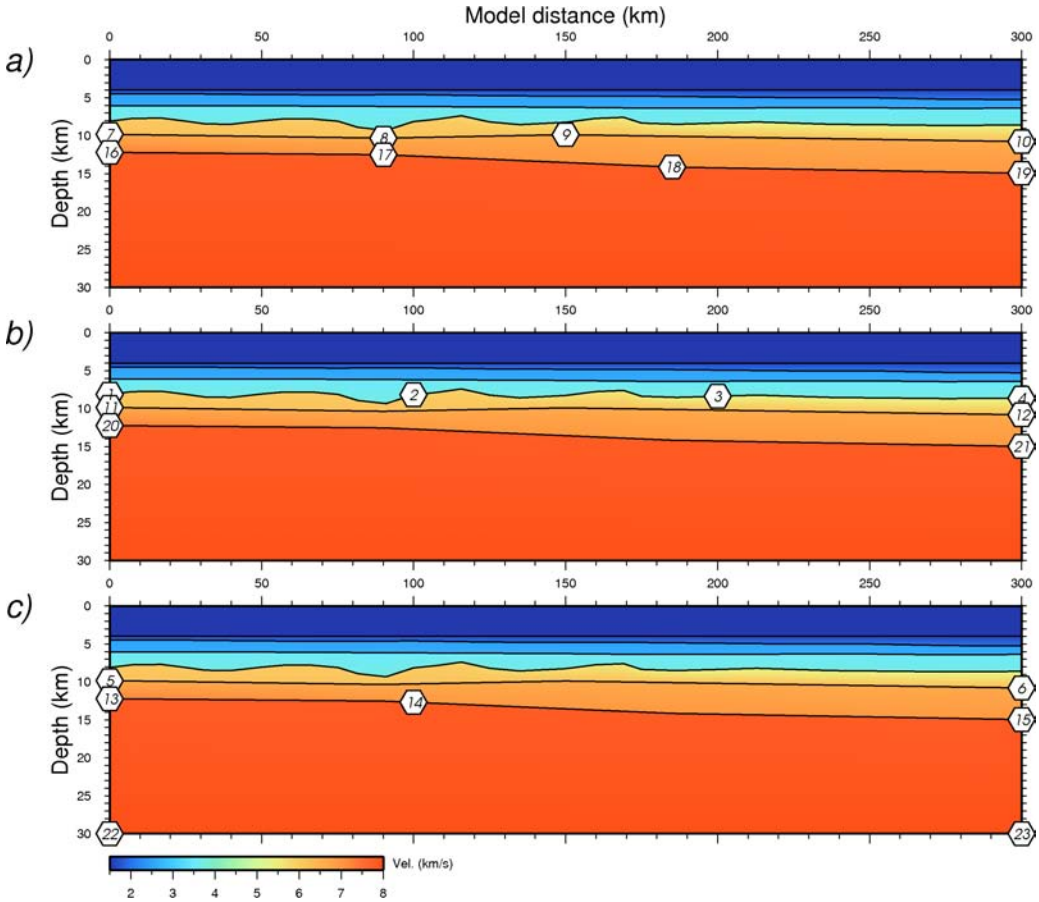

Figure 6: Oceanic basin synthetic data example, after convergence of the inversion process. Tested parameters location (white hexagons) is indicated by their ordinal in the model. *a*) depth parameters; *b*) top of layer velocity parameters; *c*) base of layer velocity parameters. Interfaces indicated by black lines and velocities coloured according to colour scale.

Maximum parameter uncertainties (negative and positive) are established by the smaller perturbation value that causes any of the four thresholds to be exceeded (limit of shading in Figure 7). As an example, parameter no. 14, which defines a velocity at the base of the second crustal layer, allows values of 7.02 ± 0.35 km/s without exceeding the previously defined thresholds. The complete results are depicted in Table 2.

In cases where ray coverage is poor, with unfavourable ray-crossings or ray-paths sub-parallel to the interfaces, the single parameter test may give suspiciously small uncertainty values. In these cases it is advisable to establish a larger uncertainty. Similarly, if a single parameter has very good ray coverage, and the calculated uncertainty is very small, it may indicate that the inversion algorithm is trapped in a local minimum and, when in doubt, the uncertainty value should also be increased. In all other cases, if uncertainties are within the reasonable bounds dictated by experience, they can be used unchanged. It is important to remember that increasing the parameter uncertainties to explore expands the model space to explore by the Monte Carlo routine.

For the current model, good candidates for increase would be the parameters defining the velocities at the top of the mantle (Table 2, parameters no. 20 and no. 21), although different results are not expected as we know the *true model*, and they were also used unchanged.

3.2. Monte Carlo simulation

VMONTECARLO (step 3, from Figure 5) was then run for a first time to test the adequacy of the RMU bounds. 40 000 random models were created, and none was rejected. Rejected models are those that are formally valid but unsuitable for ray-tracing due to unusual layer geometries or velocity gradients.

If layer pinch-outs are present in the model, they can be kept unchanged by allowing no variations of their depth nodes, or the depths of the pinch-out node on the lower layer can be bound to the corresponding nodes of the upper layer. This binding is achieved via flags in the velocity model input file.

The highest calculated score for the random models was of 0.824, corresponding to 16 587 rays and a χ^2 value of 1.720. With no need to revise the bounds due to a large number of rejected models, another 200 000 models were generated, with only one rejected. In this run, the highest calculated score was of 0.821, corresponding to 16 533 rays and a χ^2 value of 1.705. It should be noted that the second run had a number of simulations five times larger than the first, but the highest scores are very similar. As the number of simulations tends to infinity, we will converge to the true probability distribution of the models, but it is still unknown what is the minimum number of simulations to adequately characterise it (Mosegaard & Tarantola, 1995).

During the simulation, most of the generated models are tested and simply discarded when their score is too low. Only their score is saved to build figures. Models with a minimum quality, defined by score, number of traced rays, χ^2 or RMS, are saved to disk to later build a global uncertainty map.

VMONTECARLO only generates formally valid models, avoiding crossing layers, but this does not mean that the model is always suitable for ray-tracing — very complex geometries and numerical approximations may break the ray-tracer. It also incorporates the RAYINVR ray-tracing routines directly into the code, using shared modules instead of common blocks for better memory management, and removing all the overhead from the plotting and message printing routines.

The program is written as a single thread routine with the ray tracer running as an external process. There are no special CPU requirements, as with modern processors the main bottleneck will always be the reading and writing to disk. Maximum RAM usage is limited to a 32-bit address space (4 Gb).

3.3. Uncertainty estimation

To translate the estimate of the uncertainties at a specific depth into a number (step 4, from Figure 5), we set a threshold at 95% of the maximum normalised average scores (Figure 3a — horizontal black dashed line). This threshold is the result of the F-test study in section 7. The crossing of this line with the normalised average score cross-sections allows us to read the uncertainty directly from the horizontal axis (Figure 3a — vertical dashed lines). In this example, the P-wave propagation velocity at 9 km depth (upper crust, line AB) can vary between 5.05 and 5.85 km/s without reducing the average model scores by more than 5%. With shape factor $\psi = 1$, this translates into an increase of 5% of the χ^2 value while keeping the same number of traced rays, or maintaining the χ^2 value a reducing the number of rays by 95%. On the other hand, in the mantle, at a depth of 25 km (line GH), to have models with similar scores, the velocity is limited to the interval between 7.85 and 8.05 km/s.

Interface depths can also be constrained in this manner. In Figure 3c the transition between the upper and the lower crust (line KL) can vary roughly between 10 km and 11 km, and the mantle depth can vary between 14 km and 15 km (line MN) without large changes in model quality.

The distribution of maximum scores (Figure 4) can highlight heterogeneities or local maxima for the model score. In this case, due to the relative homogeneity of the model, scores vary smoothly, with higher scores centred around the preferred model.

3.4. Global uncertainty map

The ensemble of best models (step 5, from Figure 5) is a subset from the ME, where all $M^{(i)}$ models have the number of traced rays (nr), score (f), RMS and χ^2 values within certain thresholds, and can be expressed by Equation 10. The reference (Ref) values are based on the preferred model's corresponding values multiplied by the operator-chosen constants k_1, k_2, k_3, k_4, depending on the minimum quality of models we intend to classify as best models.

$$M^{(i)} \in \text{Best models} \quad \text{if} \quad \begin{cases} RMS^{(i)} \leq RMS^{(Ref)} & [RMS^{(Ref)} = RMS^{(0)} \cdot k_1] \\ \chi^{2(i)} \leq \chi^{2(Ref)} & [\chi^{2(Ref)} = \chi^{2(0)} \cdot k_2] \\ f(nr, \chi^2)^{(i)} \geq f(nr, \chi^2)^{(Ref)} & [f(nr, \chi^2)^{(Ref)} = f(nr, \chi^2)^{(0)} \cdot k_3] \\ nr^{(i)} \geq nr^{(Ref)} & [nr^{(Ref)} = nr^{(0)} \cdot k_4] \end{cases} \tag{10}$$

VMONTECARLO exported 29 917 models that were capable of tracing at least 90% of the preferred model's rays, with RMS and χ^2 values under 0.099 and 2.31, respectively, and a score value of at least 0.795. Because generating the random models is the most time-costly operation, these thresholds can be more permissive, in order to accept more models, and results filtered afterwards.

This subset was processed to obtain a global uncertainty map (step 7, from Figure 5), showing the maximum and minimum velocity deviations from the preferred model (Figure 8). Areas with small permissible velocity deviations are deemed to be well constrained because no model within the quality thresholds allows larger values.

As noted in 3.1, due to the fact that the RMU was defined from the single parameter test results, without further intervention, the velocities at the top of the mantle are not permitted to vary more than ±1.0 km/s from the preferred model's values (Table 2), greatly limiting the explorable solution space. This effect is apparent in Figure 8, where the velocities in the mantle appear to have uncertainties greater than ±0.10 km/s only in the deeper regions. They are artificially limited by the too conservative RMU bounds, but this issue can be mitigated if the allowed parameter variations are previously checked for too small values, or if the RMU bounds are defined via a less conservative approach.

3.5. Parameter values histograms

The final output of VMONTECARLO is a collection of histograms (step 6, from Figure 5, and Figure 9) for the values taken by each parameter of interest in the best models subset. The same models used to create a global uncertainty map are used to obtain the distribution of acceptable values each parameter can assume in models that properly fit the data.

This output does not address the parametrisation suitability of the model, nor the lack of ray coverage or smearing for a specific parameter. It does, however, allow for a more detailed analysis of the expected uncertainty of each parameter, such as symmetry of the distribution and preferred values.

From the analysis of the histograms (Figure 9), we can conclude that some parameters are well constrained, for example parameters no. 9 (top of lower crust depth, Figure 9b) and no. 12 (velocity at the top of the lower crust, Figure 9d) with a higher model count around a specific value and well-marked, almost symmetrical decays to each side. This means that, from the collection of acceptable models, a specific parameter value was more probable than others. Some parameters show an asymmetrical count decay to each side of a the preferred model's value as, for example parameter no. 23 (mantle velocity at the base of the model, Figure 9f), where the peak of the histogram is very close to the unperturbed value but acceptable random models with negative perturbations are much less probable than with positive perturbations.

Some parameters seem to be not as well constrained by the observations, because it is harder to define an obvious peak in the histogram, meaning that acceptable random models are not very dependent on the value of these parameters. Two examples are parameters no. 7 (top of lower crust depth, Figure 9a) and no. 1 (velocity at the top of the upper crust, Figure 9c), where the maximum

and minimum model counts are not very different — although a curve could be fitted to help the interpretation.

Other parameters do not show a preferred solution but do show that there exists a limit where values are less probable, such as parameter no. 13 (velocity at the base of the lower crust, Figure 9e), where higher velocities are much less probable.

It should be noted that the highest count on the parameter's histograms may not coincide with the preferred model's value, even if the preferred value is obtained by inversion. This is due to VMONTECARLO not being sensitive to any global constraints other than the RMU, which it discretely samples, meaning that it may fail to find solutions similar to the preferred model's, and that these solutions may highlight different local maxima than those obtained by inversion from a given starting model. It is also known that different starting models may lead to different inversion results if they are close to local minima (Zelt & Smith, 1992). An additional remark is that VMONTECARLO uses a finite number of samples in an attempt to extract meaningful information from a model space that, for any practical purpose, is infinite.

3.6. Distribution of scores

In Figure 3b, red colours in narrow bands indicate low velocity dispersion and uncertainty, and magenta colours in large bands indicate high velocity dispersion and uncertainty. The maximum scores plot (Figure 4) is useful to highlight models that best fit the data, identify potential alternate solutions, and compare them to the tested solution. Maximum and normalised average score scales are not comparable. In these figures, the preferred and best random models are quite different in the first crustal layer, where a velocity gradient is replaced by an abrupt velocity change while keeping comparable score. This highlights that for the given quality thresholds, it is possible to fit data with very different models.

The normalised average scores plot can also provide an approximation to the probability distribution of the propagation velocity as a function of depth (Figure 3b). Due to the non-linearity of the problem, this distribution is not expected to be Gaussian or even symmetrical. Cross-sections of this distribution at specific depths are histograms of propagation velocity versus normalised average score (Figure 3a) and help give further insight to the spread of the solutions. Flat curves indicate large dispersion of solutions, but well defined maxima indicate well-constrained solutions.

In this example, the dispersion of high scores around the preferred model is smaller mainly in the top of the mantle layer (Figure 3b, at about 15 km depth), showing that a model that fits the data well must have mantle velocities in that range. This indicates that the velocity at that point has a small uncertainty. The velocity uncertainty increases for all the remaining depths. This result is

quite clear from the curves in Figure 3a: the wide flat curve CD of the distribution of the normalised average scores in the lower crust indicates a large number of possible solutions, as model score decays slowly when we move away from the preferred model. The narrow curve EF of the distribution of the average scores in the top of mantle indicates a smaller number of solutions, as noted earlier.

In the mantle, the normalised average scores distribution shows an abrupt decay, with an asymmetrical distribution, which could indicate a different velocity gradient, but by observation of the shape of the curves (Figure 3a — lines EF and GH), especially the curve at 25 km depth, an almost flat top indicates that the gradient is resolved within the data uncertainty.

The lower crust, on the other hand, seems to have a larger uncertainty around the preferred model, as the width of the red area is significantly larger than that of the upper crust, but the distribution of the average scores (Figure 3a — line CD) suggests that there is less uncertainty, i.e., model score decays faster as it moves away from the better solutions. It should be noted that the distribution around the preferred model is also not symmetrical.

In Figures 3b and 4, the preferred model's 1D profiles cross the higher scores areas, and the best random model has a score of 0.823, which is comparable to the preferred model's original score. This indicates that VMONTECARLO was ran with an adequately sized ME, and that the preferred model is a good solution.

3.7. Pinch-out handling

Most RAYINVR velocity models present interfaces pinching out, and these can pose problems for Monte Carlo methods if no extra constraints are given. VMONTECARLO, other than the RMU limits defined by the user, does not impose constraints on the velocity gradients or relative layer distances when generating random models. Generally, pinch-out structures are handled as any other parameter and allowed to freely and independently vary within the RMU, or their depth parameters can be linked via a flagging system during the generation of random models to keep the pinch-out in the model.

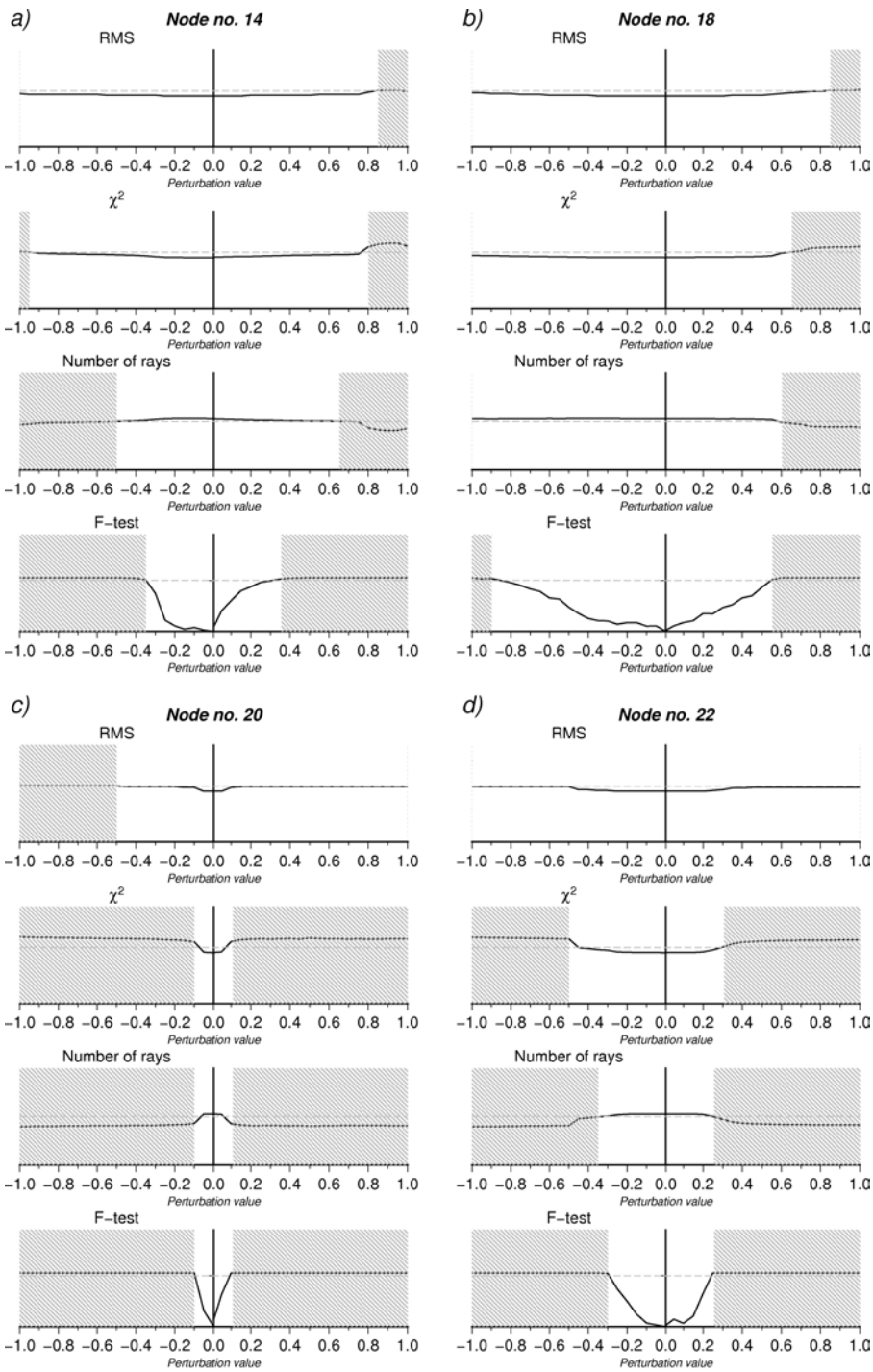

Figure 7: Single parameter test results for the synthetic data. *a*) (from top to bottom) Model RMS, χ^2, number of traced rays and F-test confidence level for perturbations of parameter no. 14 (velocity of bottom of lower crust layer), after eight inversion iterations. Black line — model RMS/χ^2/number of rays/F-test confidence level; dashed grey line — thresholds for RMS/χ^2/number of rays/F-test 95% confidence level; shading — model RMS/χ^2/number of rays/F-test exceeded its threshold. Parameter error is established by the smaller perturbation exceeding a threshold: -0.35 km/s and +0.35 km/s from F-test. *b*) Same as a for node 18 (Moho depth). Depth error bounds are: -0.90 km and 0.55 km, established from F-test; *c*) Same as a for node 20 (velocity of top mantle layer). Velocity error is ± 0.1 km/s, established from F-test, number of rays and χ^2. *d*) Same as a for node 22 (velocity of bottom mantle layer). Velocity error bounds are -0.30 km/s, established from F-test, and +0.25 km/s, established from F-test and number of rays. Parameter node location in given in Figure 6.

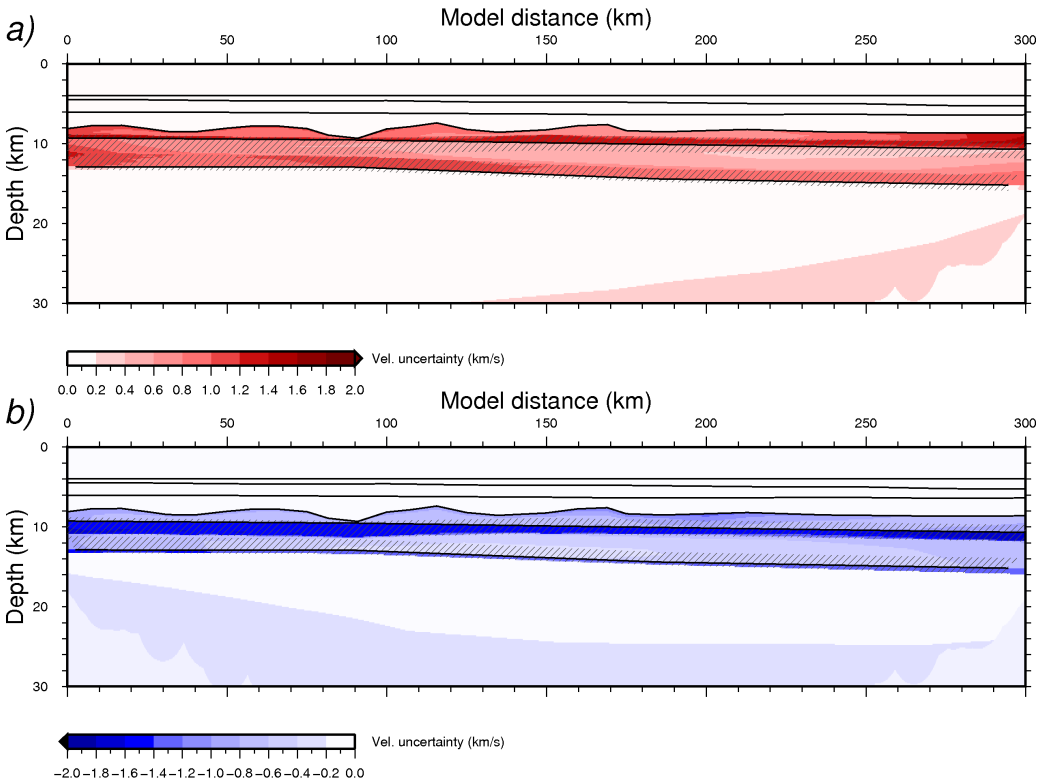

Figure 8: Global uncertainty plot. *a*) Maximum and *b*) minimum admissible velocity deviations from the preferred model, built from 29 917 models within the quality threshold. Preferred model's interfaces are indicated by black lines and velocity deviations are coloured according to colour scales. The best random model's interfaces are indicated by dashed lines. Hatched regions around interfaces indicate maximum interface depth variations, as defined in section 3.1.

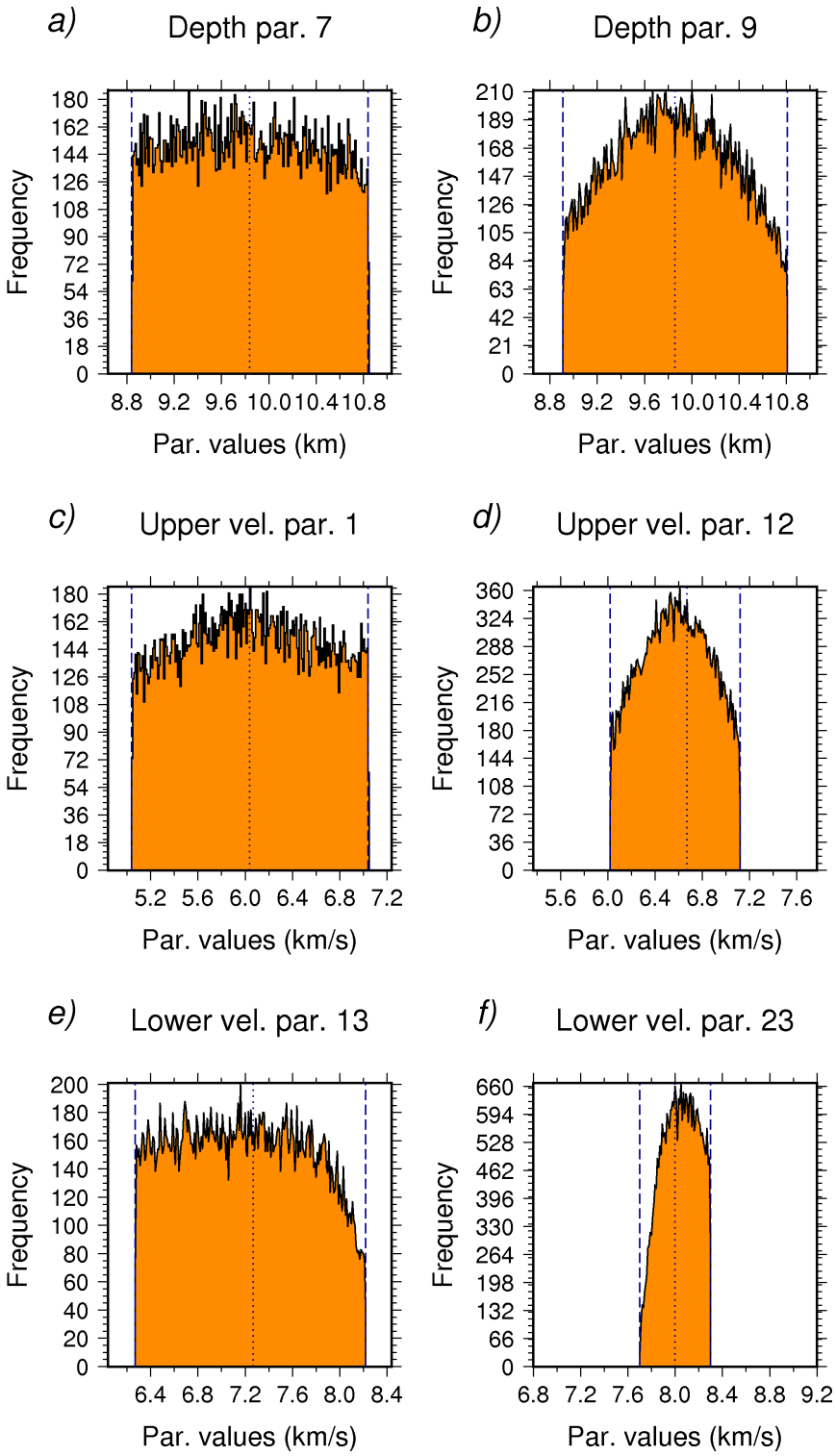

Figure 9: Histograms of parameter values of acceptable models for the synthetic example. *a*) Distributions of values of acceptable models for middle crust depth parameter no. 7. *b*) Same as a for parameter no. 9. *c*) Distribution of top of upper crust velocity values for parameter no. 1. *d*) Distribution of top of lower crust velocity values for parameter no. 12. *e*) Distribution of base of lower crust velocity values for parameter no. 13. *f*) Distribution of base of model mantle velocity for parameter no. 23. Vertical pointed black line indicates preferred model's value. Vertical dashed blue lines indicate RMU bounds for the given parameter. Parameter location is given in Figure 6.

4. Results

VMONTECARLO was applied to 250 km sections of SB01 and SB02 (Figures 1d and 1e), corresponding to the studied central region of the Santos Basin, where an accurate geological interpretation depends greatly on the uncertainty assessment of the velocity model. Resolution tests and ray coverage for profiles SB01 and SB02 are available as supplementary material in (Evain et al., 2015).

The Santos Basin/São Paulo Plateau is mostly underlain by thin continental crust, but there is a v-shaped central region showing an atypical structure interpreted as an abandoned oceanic ridge with the rifting oblique to the opening direction of the South-Atlantic (Moulin et al., 2012). This model, although already tested with other techniques, is a good candidate for the application of VMONTECARLO due to the atypical structures imaged, as alternate valid solutions may lead to different geological interpretations. None of the methods previously used provided information about alternate models.

The extracted section of the SB02 profile is better constrained by arrivals from the deep crust than the corresponding section of SB01. It is capable of tracing 10 701 rays to 22 133 observations, with a RMS value of 0.127, and a χ^2 value of 1.441. The discrepancy between the number of rays and observations is due to the inclusion of pre-basement observations, which are not evaluated as they are well constrained independently, but as VMONTECARLO integrates directly in the normal modelling work-flow, all the measured travel times were used. These values correspond to a score of 0.452 when using shape factor $\psi = 1$ on Equation 7. Defining quality of fit via the scoring function is useful for later comparison with the generated models. The discrepancy between the number of traced rays and observations is due to the fact that only crustal arrivals were studied and the observations file also includes data for the sedimentary basin. This does not affect the results or conclusions, as the extra number of observations only affects the score calculation.

4.1. Random models universe

On this model, single parameter uncertainty tests assign a very low uncertainty to several parameters due to the peculiar geometry of the Moho uplift and the missing distal and proximal sections of the profile. To avoid a biased uncertainty test, we chose not to use these values and increase the allowable parameter variations to ±1.00 km or ±1.00 km/s on all parameters of interest. This RMU encompasses eventual local minima obtained from the single parameter uncertainties and it covers most of the expectable uncertainties for these parameters (Stratford et al., 2009, for example). Expanding the model space requires a greater number of random models in order to adequately sample it and produce meaningful results. The minimum number is unknown, but based on trial and error, we estimate that 100 000 random models are enough to adequately sample the RMU of SB02. Figure

10b shows the location of the 33 studied parameters. As in the synthetic example, sedimentary layers parameters and basement geometry are excluded.

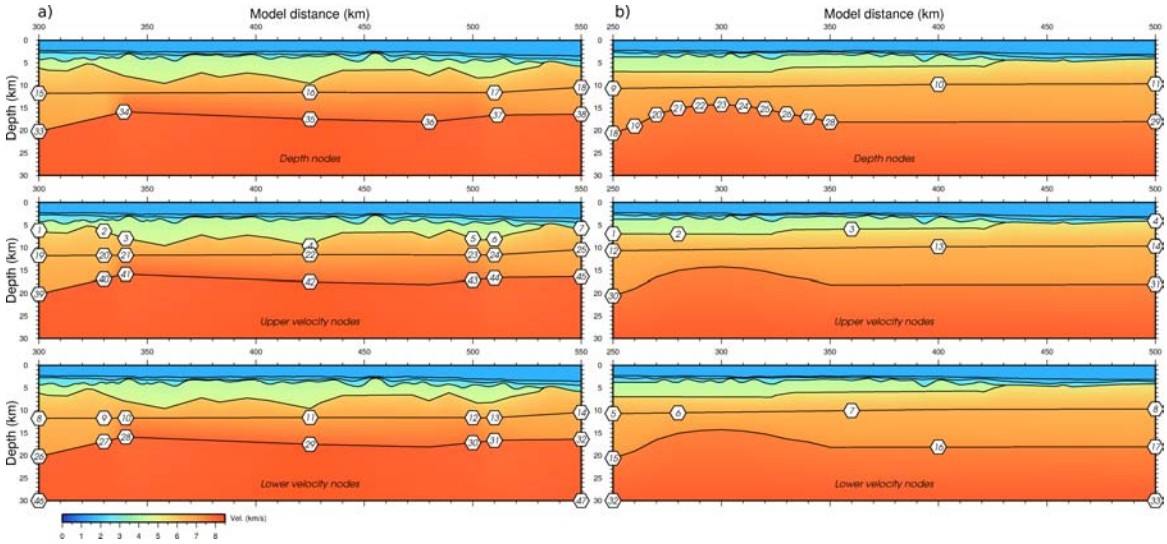

Figure 10: Studied excerpts of *a*) SB01 and *b*) SB02 profiles. Tested parameters location (white hexagons) is indicated by their ordinal in each the model. (Top panels) depth parameters; (Middle panels) top of layer velocity parameters; (Bottom panels) base of layer velocity parameters. Interfaces indicated by black lines and velocities coloured according to colour scale. Profile locations is given in Figure 1a). Adapted from Evain et al. (2015).

The maximum and minimum allowable parameter values define a universe of models having similar or higher ability to fit the data set than those of the preferred model. If they are set too small, the model space is not effectively explored and valid solutions may be discarded. On the other hand, if they are over-estimated, calculation time increases as a larger number of simulation is needed. To reach a similar sampling of the model space on a larger RMU, the number of stochastic models must increase.

4.2. Distribution of scores

A Monte Carlo simulation of 500 000 models resulted in a ME of 499 985 models, with 1D velocity-depth profiles plotted at each 20 km on every model. Figure 11b shows the normalised average scores for profiles at 350 km model distance. Horizontal cross-sections highlight the distribution of the random model's scores around the preferred model. It should be noted that due to the Moho uplift, ray coverage of the upper mantle (as described in Evain et al. (2015)) is not ideal, resulting in a poor constrain of the mantle velocity gradient. This is evident on cross-section GH (Figure 11a), where changing mantle gradients has no discernible effect on the average scores of models.

The horizontal cross-sections AB, CD and EF (Figure 11a) show a good constraint of the velocity field at their respective depths. The vertical cross-section KL (Figure 11c) indicates that the interface depth is at a local maximum of the average scores, and cross-section MN shows a wide, flat maximum

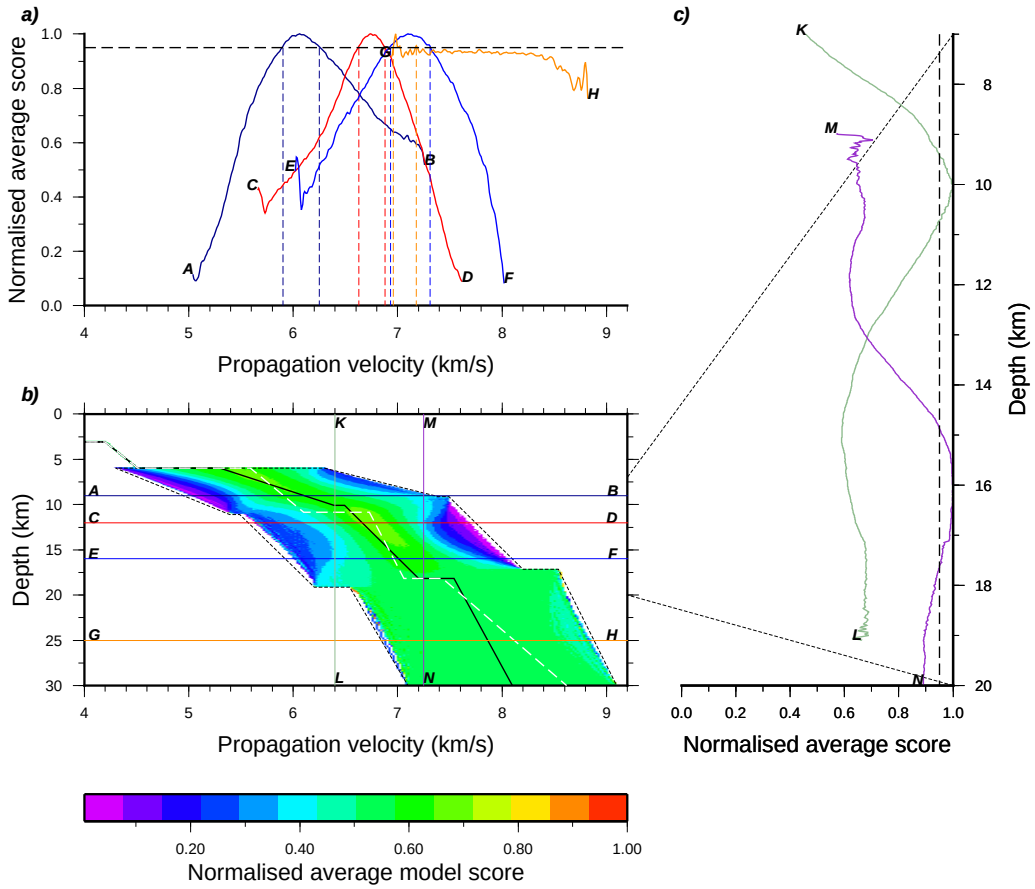

Figure 11: Normalised average models scores distribution at 350 km model distance. *b*) Average models scores distribution of the entire dataset. Thin dashed lines mark independent parameter uncertainties. Solid black line indicates tested model. Dashed white line indicates best random model. Letters A to H, and K to N mark the location of the horizontal and vertical cross-sections of the average scores distribution shown in *a*) and *c*). *a*) Cross-sections of normalised average scores distribution at different depths, highlighting layer velocity gradients, with colours and letters matching the horizontal lines in *b*). Black horizontal dashed line indicates 95% of the maximum normalised average score, corresponding to the score of a model capable of tracing 95% of the original number of rays and with an increase of 3% of the original χ^2. Vertical dashed lines indicate the uncertainties at this level for the corresponding colours. *c*) Cross-sections of average scores distribution at different velocities, highlighting interface depths, with colours and letters matching the vertical lines in *b*); vertical dashed black line indicates 95% of the maximum normalised average score.

indicating a large number of equally acceptable solutions. In this case, the best random model gives additional confidence on the preferred model's depth as they are coincident.

Figure 12 shows the grouping of the maximum scores at each pixel. The insufficient data coverage in the mantle is highlighted by the dispersion of the maximum model scores at around 0.45 across almost the entire range of the permissible parameter values. On the crustal layers, the maximum scores are grouped much closer to the preferred model's values. Information from this figure can be used to further refine the *RMU* bounds on additional VMONTECARLO runs, for example, by reducing the maximum allowable parameter values in the areas of the graph where the maximum model scores are significantly lower.

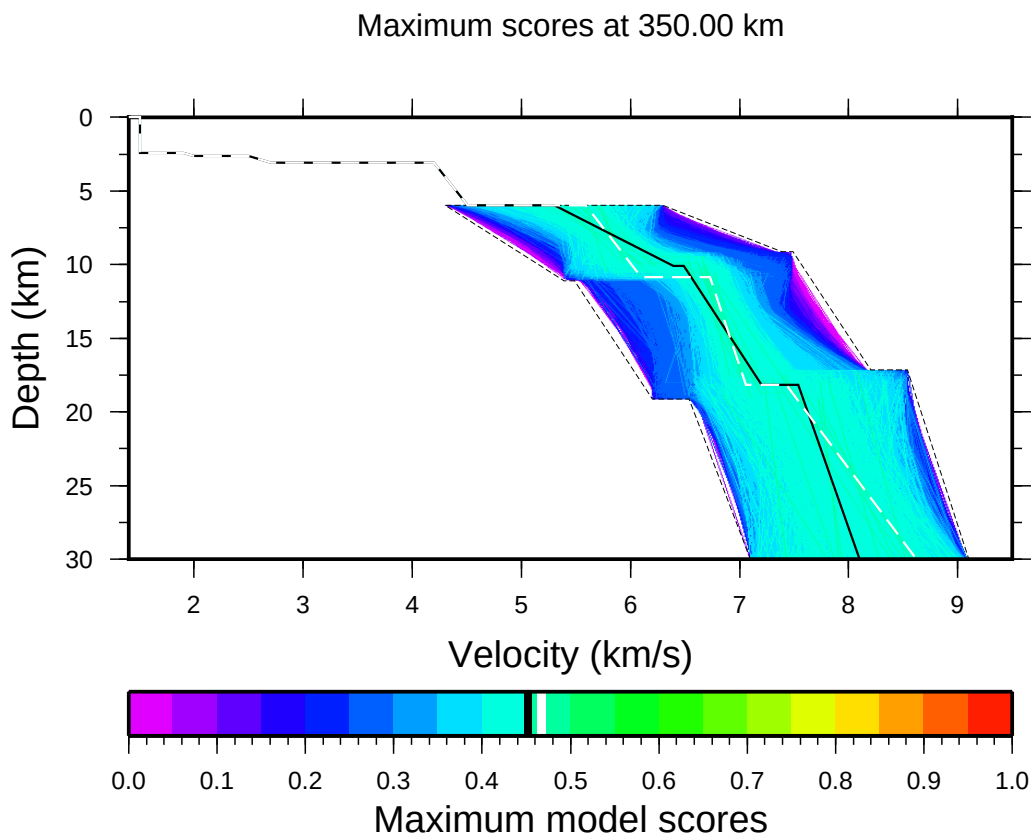

Figure 12: Maximum model scores distribution at 350 km model distance of the entire dataset. Black solid line indicates tested model. Thin dashed lines mark RMU bounds. White marker on scale indicates score of best random model. Black marker on scale indicates score of tested model.

4.3. Global uncertainty map

The best models from the ME are chosen if they meet the quality thresholds defined by Equation 10, and are based on the quality of fit of the preferred model. For this model we established the following thresholds: *a*) RMS value not exceeding by more than 15% the preferred model's value ($RMS^{(Ref)} = RMS^{(0)} \cdot 1.15 = 0.146s$); *b*) χ^2 value not exceeding by more than 50% the preferred model's value ($\chi^{2(Ref)} = \chi^{2(0)} \cdot 1.5 = 2.16$); *c*) number of traced rays not less than 90% of the preferred model's traced rays ($nr^{(Ref)} = nr^{(0)} \cdot 0.9 = 9630$) and *d*) score not below 90% of the preferred model's score ($f(nr,\chi^2)^{(Ref)} = f(nr,\chi^2)^{(0)} \cdot 0.9 = 0.4068$). The chosen reference values for RMS and χ^2 would be expectable in models with an average fit, which is plausible given the complexity of the imaged structures.

From the ME, 254 models met the quality thresholds, and were used to build Figure 13, where the velocity model is gridded and at each cell location the maximum and minimum depth and velocity deviations from the preferred model's values are calculated from this subset of models. This means that we have a global measure of uncertainty for the profile. At any given location we can estimate how much the preferred model's velocity can vary without exceeding any of the previously imposed quality of fit thresholds.

The results obtained on the real data set shed light on the quality of the profile's velocity model and allow much more meaningful geological interpretations, as it is possible to exclude some types of alternate solutions. But, in some cases, this method can allow alternate interpretations if the calculated uncertainties are large enough.

5. Discussion

Careful analysis of Figure 13 shows that there is higher velocity uncertainty around the interfaces. This is due to velocity-depth trade-off effects. Different models may have the same interface at different depths and thus, the same cell can have velocities sampled from the layer above or below.

These uncertainty bounds are calculated from a set of models that do not exceed the defined quality thresholds. Physical or geological validity is not tested, and therefore it is possible that there are models within these bounds with velocity inversions or strong vertical or lateral gradients. Models obtained from inversion may also suffer from the same limitations if the algorithm converges to a local minimum when the model to invert is not already close to the solution.

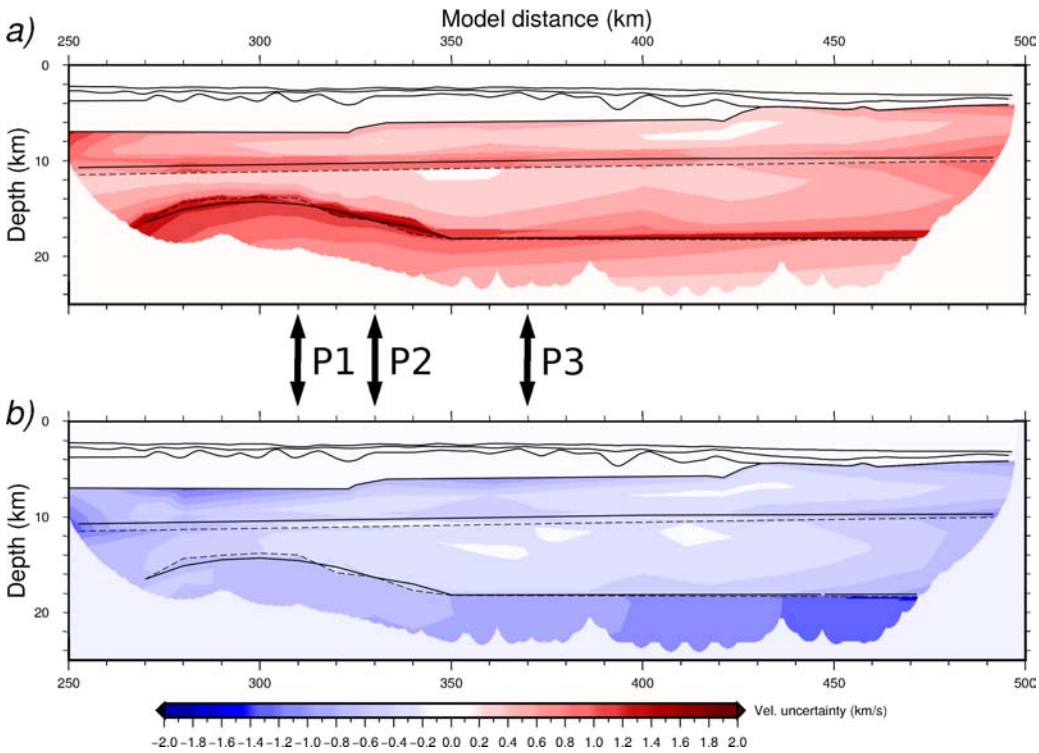

Figure 13: Global uncertainty plot for SB02. *a*) Maximum and *b*) minimum admissible velocity deviations from the preferred model, built from 254 models within the thresholds defined in Section 4.3. Shaded areas indicate ray coverage. Preferred model's interfaces are indicated by black lines and velocity deviations are coloured according to colour scales. The best random model's interfaces are indicated by dashed lines. Vertical black arrows and P1, P2, and P3 mark the locations of compared 1D velocity-depth profiles.

The corresponding section on SB01 is characterized as not having clear PmP arrivals and thus no evidence of Moho discontinuity. Because of this, the modelling strategy was different from the

one used on SB02, as travel times alone are insufficient to constrain velocity gradients and interface depths. For SB01, amplitude information and synthetics were the main tools used to image the deep crust and mantle.

For SB01 we ran a simulation of 500 000 models and generated a ME of 499 899 models. To calculate the global uncertainty map, the thresholds were set as follows: *a*) RMS value not exceeding by more than 15% the preferred model's value ($RMS^{(Ref)} = RMS^{(0)} \cdot 1.15 = 0.160s$); *b*) the same χ^2 value as in SB02 ($\chi^{2(Ref)} = 2.16$ – Section 4.3); *c*) number of traced rays not less than 90% of the preferred model's traced rays ($nr^{(Ref)} = nr^{(0)} \cdot 0.9 = 5357$) and *d*) score not below 90% of the preferred model's score ($f(nr,\chi^2)^{(Ref)} = f(nr,\chi^2)^{(0)} \cdot 0.9 = 0.2584$). Only 35 models met these quality thresholds, confirming that travel times are insufficient to adequately model the deep crust. VMONTECARLO indicates high uncertainties for depths and velocities in this region of SB01 (Figure 14). However, taking into account the uncertainties of both profiles, we can say that the structures are indeed different in both profiles even when using only travel times.

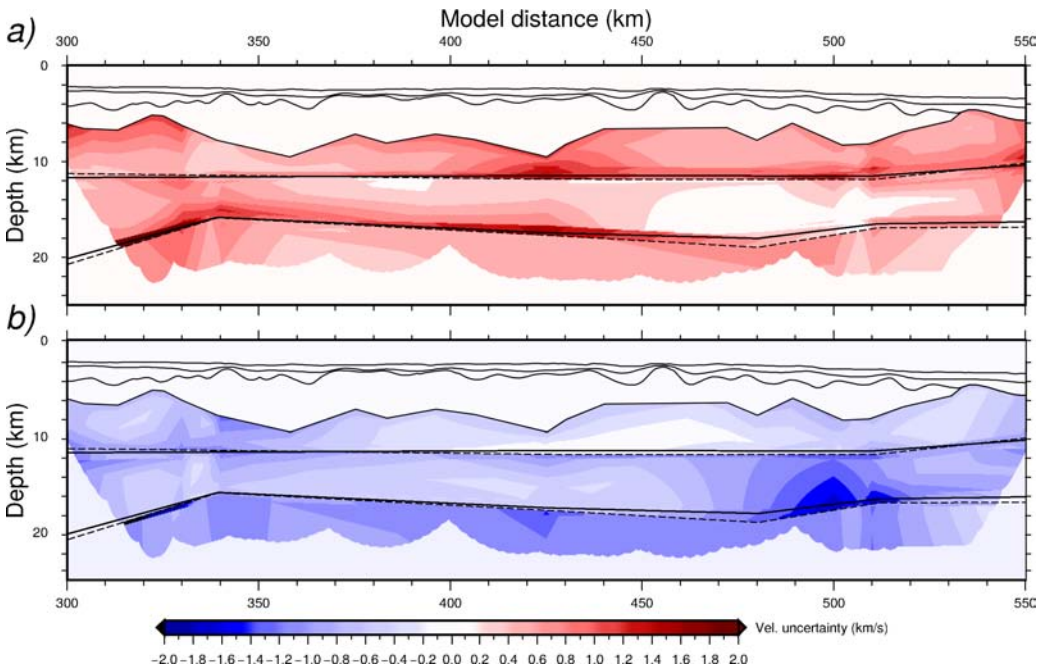

Figure 14: Global uncertainty plot for SB01. *a*) Maximum and *b*) minimum admissible velocity deviations from the preferred model, built from 35 models capable of tracing at least 5 357 rays, with an RMS value under 0.160 *s* (115% of the preferred model's) and a χ^2 not exceeding 2.16 (the same quality of fit threshold used for SB02 in Figure 13). Shaded areas indicate ray coverage. Preferred model's interfaces are indicated by black lines and velocity deviations are coloured according to colour scales. The best random model's interfaces are indicated by dashed lines.

Acquisition geometry and ray coverage were equivalent in both profiles, but in the studied domain, ray density in the lower crust is lower in SB01 than on SB02 (as described in Evain et al., 2015).

5.1. Robustness of results

Figure 14 shows the global uncertainty map for profile SB01, using the same quality thresholds as in SB02 (Figure 13). Figure 10a shows the location of the 47 studied model parameters for profile SB01.

With only refracted arrivals from the lower crust and upper mantle, and no clear PmP arrivals, it is quite difficult to generate good random models. This difficulty is mostly due to the fact that reflections are only dependent of velocity contrasts between layers, but refractions are very sensitive to gradient variations.

It is clear that, using travel times alone there is great uncertainty in the velocities in the lower crust/upper mantle transition, even with a sample of only 35 models. There are regions in the lower crust where acceptable models are more likely to admit lower velocity values than higher, for example at 500 km model distance and 15 km depth. This case is an example where the preferred model could be updated based on the results of VMONTECARLO.

If the threshold quality levels for RMS and χ^2 are relaxed to 130% and 150% of the preferred model's values, respectively, admitting a larger number of models (and thus increasing sample size), the maximum uncertainties are larger, as expected, but their distribution remains roughly the same, as it is evident from the comparison between Figure 14 (using 35 models) and Figure 15 (using 151 models). The relaxed quality thresholds are not too permissive, as they still required that models have an acceptable fit ($\chi^2 = 2.269$).

On SB02, using the 254 best models as an approximation to the parameter values distribution, we generated histograms to infer about the quality of the preferred model and the suitability of the RMU. The distribution of the solutions around the preferred value without a large dispersion, as seen in the upper velocity parameters (Figures 16e through 16h), which are constrained directly by apparent velocities of refracted arrivals, is evidence that the preferred model is a good solution.

Base velocities and gradients are harder to constrain without using amplitude information, but on this profile, they show that the best models have velocities around the preferred solution and, in the case of parameter no. 7 (velocity at base of upper crust, Figure 16i), there is a limit to the maximum value it can take with exceeding the previously defined quality thresholds.

With a relatively small number of accepted models and the influence of the velocity-depth trade-off on the depth of interfaces, the interpretation of the histograms for the depth parameters is harder, as the histogram values are very scattered, meaning that for the allowed variations of each parameter, the number of simulations was not enough to clearly establish a preferred value. This is expected, as velocities are easier to constrain than interface depths. In some cases, such as in parameter number 26 and even with a limited number of simulations, the grouping of peaks suggests that depth uncertainty

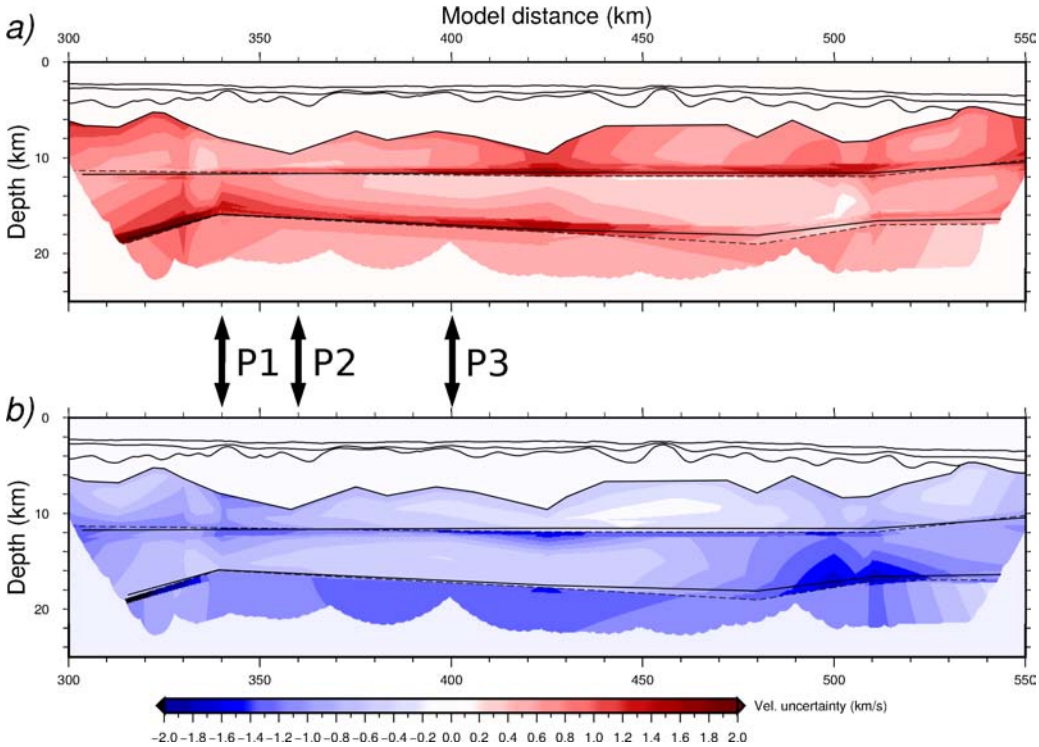

Figure 15: Global uncertainty plot for SB01. *a*) Maximum and *b*) minimum admissible velocity deviations from the preferred model, built from 151 models capable of tracing at least 5 357 rays (90% of the preferred model's), with an RMS value under 0.180 s (130% of the preferred model's) and a χ^2 not exceeding 2.269 (150% of the preferred model's). Shaded areas indicate ray coverage. Preferred model's interfaces are indicated by black lines and velocity deviations are coloured according to colour scales. The best random model's interfaces are indicated by dashed lines. Vertical black arrows and P1, P2, and P3 mark the locations of compared 1D velocity-depth profiles.

is most likely not symmetrical around the preferred value, with a bias towards larger values (deeper interface).

In Figure 3b, red colours in narrow bands indicate low velocity dispersion and uncertainty, and magenta colours in large bands indicate high velocity dispersion and uncertainty. The maximum scores plot (Figure 4) is useful to highlight models that best fit the data, identify potential alternate solutions, and compare them to the tested solution. Maximum and normalised average score scales are not comparable. In these figures, the preferred and best random models are quite different in the first crustal layer, where a velocity gradient is replaced by an abrupt velocity change while keeping comparable score. This highlights that for the given quality thresholds, it is possible to fit data with very different models.

The normalised average scores plot can also provide an approximation to the probability distribution of the propagation velocity as a function of depth (Figure 3b). Due to the non-linearity of the problem, this distribution is not expected to be Gaussian or even symmetrical. Cross-sections of this distribution at specific depths are histograms of propagation velocity versus normalised average score (Figure 3a) and help give further insight to the spread of the solutions. Flat curves indicate large dispersion of solutions, but well defined maxima indicate well-constrained solutions.

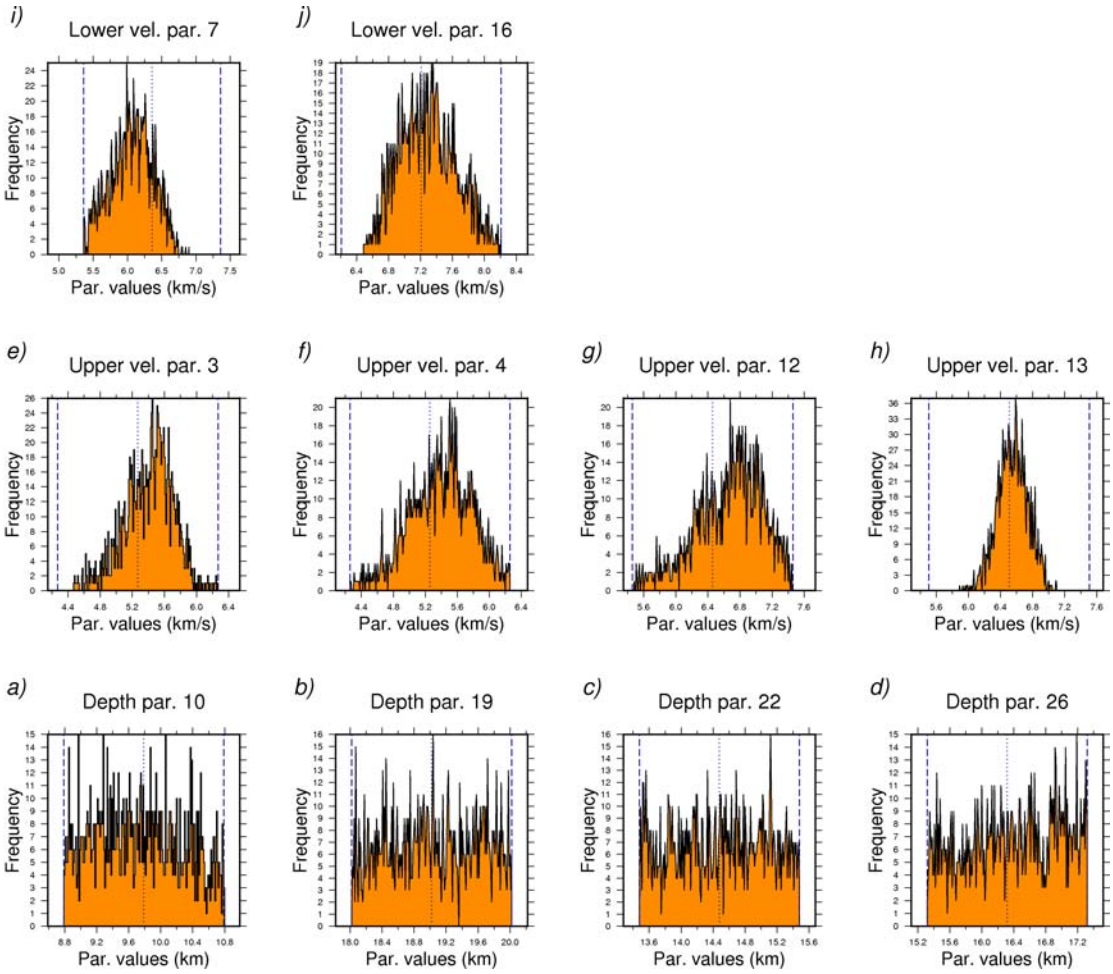

Figure 16: Histograms of parameter values of acceptable models for SB02. *a*) Distributions of values of acceptable models for top of lower crust depth parameter no. 10; *b*) , *c*) and *d*) , Same as a for base of lower crust depth parameters no. 19, 22 and 26; *e*) and *f*) Distribution of velocity values at top of upper crust for parameters no. 3 and 4; *g*) and *h*) Distribution of velocity values at top of lower crust for parameters no. 12 and 13; *i*) Velocity at base of upper crust parameter no. 7; and *j*) Velocity at base of lower crust parameter no. 16. Vertical pointed black line indicates preferred model's value. Vertical dashed blue lines indicate RMU bounds for the given parameter. Parameter location is given in Figure 10b.

In this example, the dispersion of high scores around the preferred model is smaller mainly in the top of the mantle layer (Figure 3b, at about 15 km depth), showing that a model that fits the data well must have mantle velocities in that range. This indicates that the velocity at that point has a small uncertainty. The velocity uncertainty increases for all the remaining depths. This result is quite clear from the curves in Figure 3a: the wide flat curve CD of the distribution of the normalised average scores in the lower crust indicates a large number of possible solutions, as model score decays slowly when we move away from the preferred model. The narrow curve EF of the distribution of the average scores in the top of mantle indicates a smaller number of solutions, as noted earlier.

In the mantle, the normalised average scores distribution shows an abrupt decay, with an asymmetrical distribution, which could indicate a different velocity gradient, but by observation of the shape of the curves (Figure 3a — lines EF and GH), especially the curve at 25 km depth, an almost flat top indicates that the gradient is resolved within the data uncertainty.

The lower crust, on the other hand, seems to have a larger uncertainty around the preferred model, as the width of the red area is significantly larger than that of the upper crust, but the distribution of the average scores (Figure 3a — line CD) suggests that there is less uncertainty, i.e., model score decays faster as it moves away from the better solutions. It should be noted that the distribution around the preferred model is also not symmetrical.

In Figures 3b and 4, the preferred model's 1D profiles cross the higher scores areas, and the best random model has a score of 0.823, which is comparable to the preferred model's original score. This indicates that VMONTECARLO was ran with an adequately sized ME, and that the preferred model is a good solution.

The best random model is capable of tracing 11 802 rays, with a RMS of 0.138 and a χ^2 value of 1.673, resulting in a slightly higher score ($f(nr,\chi^2)^{(best)} = 0.467$) than that of the preferred model ($f(nr,\chi^2)^{(0)} = 0.452$). This higher score is due to the larger number of traced rays and comes at the cost of a slight increase of RMS and χ^2 values. It is also important to remind that the preferred model is a simple excerpt from the complete SB02 profile and no inversion of travel times of further data manipulations were performed. Parametrisation suitability or adequacy of model roughness were not re-evaluated. All edge effects and incomplete ray coverage introduced by the suppression of data to either side of the imaged structures are present. Nevertheless, and although depths and velocities were permitted to vary freely, the best random solution is remarkably close to the preferred model (see interface depths and upper crust gradient in Figure 11b, and difference between preferred and best model's interface depths in Figure 13).

The layer that overlays the crust and pinches out at 430 km model distance is an Aptian evaporitic deposit, that causes a velocity inversion. It has a noticeable influence on the uncertainty of the lower crust velocity field immediately below (Figure 13a, at 400 km model distance and 10-15 km depth). The topography of this layer has a strong effect on ray paths and there is a roughly triangular region where we can increase the lower crust's velocity by more than 0.4 km/s and still have a model with an acceptable fit.

Profile SB02 has a pronounced Moho rise at 300 km model distance (Evain et al., 2015), and VMONTECARLO shows that the model adequately characterises this structure with a small depth uncertainty.

5.2. Comparison with the single parameter uncertainty method

One of the available methods to establish model uncertainty is the single parameter uncertainty estimation Zelt (1999), where each parameter is regarded as independent and tested to determine the limits within it can vary without affecting model fit, and is commonly used to evaluate interface and

velocity uncertainties in several contexts (Karastathis et al., 2001; Plaza-Faverola et al., 2010, among others).

It is an iterative process where the parameter is perturbed with increasingly larger values, followed by inversion of the remaining parameters until convergence, while keeping the perturbed parameter fixed. Because it is an intrinsically non-linear problem, the perturbation value does not directly correlate with the number of traced rays or travel time fit and test limits must be set in a conservative manner as to accept possible local minima while responding to global trends. Furthermore, as the introduced perturbations are discrete, there is a chance that model response changes drastically with a small increment in the perturbation value. Increment size is a compromise between the ability to identify local minima and reasonable calculation times.

To illustrate the differences between the single parameter uncertainty estimation and our method, we produce two plots of all estimated velocity error bounds. These plot provide a view of the maximum perturbation that is possible to independently impose to each model parameter, splitting the minimum and maximum velocity bounds; and one plot of all estimated depth errors (Figure 17). Although all selected parameters are considered in the plot, because they are tested independently, it does not mean that a given combination of values for these parameters within their estimated error bounds will correspond to a model with acceptable fit. Instead, this plot represents jointly the extreme values that each selected velocity or depth can assume when independently varied while all other parameters remain unchanged. The colour scale is the same as the one used in Figure 8, but as no parameter was tested with a perturbation larger than ± 1.00 km or ± 1.00 km/s, the maximum allowable deviations can seem smaller. This plot does not provide a useful assessment of the model uncertainties nor the geophysical and geological constrains they may provide. The estimated error bounds for the 23 studied parameters is given in Table 2.

For the single parameter uncertainty tests, we based the criteria for acceptance of a perturbed model on the threshold of the number of rays traced, RMS, χ^2 value and significance, determined by an F-test. χ^2 values depend on RMS and number of traced rays, providing a normalised measure that includes the data uncertainty, usually estimated from the signal to noise ratio of each arrival. RMS and χ^2 values are considered because separate travel times can have different uncertainties, meaning that χ^2 values and RMS might not vary proportionally from one iteration to the next if different sets of rays are traced. As the number of observations can also vary without large changes to the RMS and χ^2 values, we need to ascertain if the perturbed model is significantly different from the preferred model with an F-test.

Other than the statistical significance of results determined by means of an F-test, it is difficult to establish objective criteria to define the model acceptance threshold values on RMS, χ^2 and number

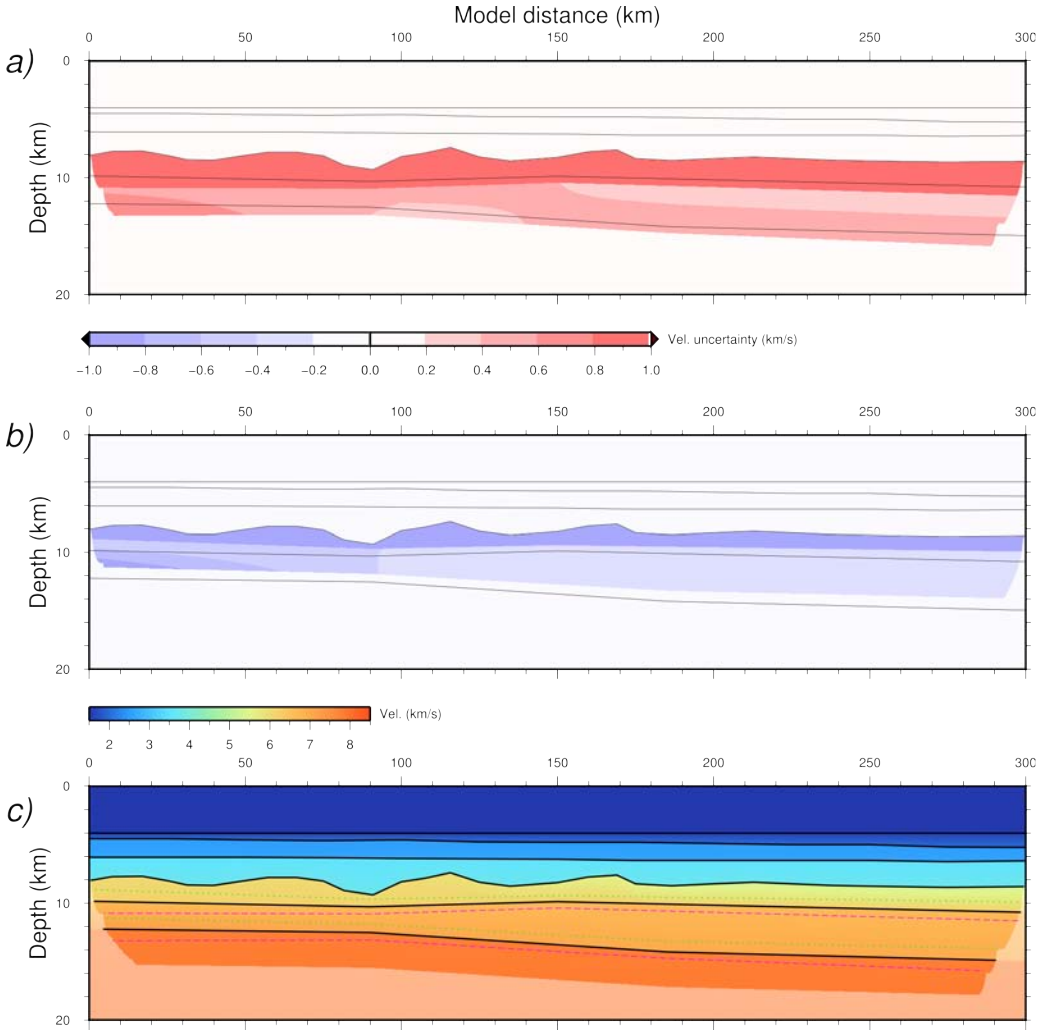

Figure 17: Global plot of single parameter uncertainties for the synthetic example in Figure 7. Each parameter is assumed independent of remaining ones, i.e., velocities and depths may assume these extreme values locally, but not simultaneously on all model locations. *a*) maximum local velocity perturbation; *b*) minimum local velocity perturbation; *c*) minimum (green dashed line) and maximum (pink dashed line) local depth of interfaces. Shaded areas indicate ray coverage. Colour scale is the same as in Figure 8. In c, solid black lines indicate unperturbed model depth of interfaces. In b and c interface depth is indicated by solid grey lines.

of rays, as they depend on the relation of complexity of the medium with the spatial resolution of the data. Tests were performed to set their appropriate values. A minimum number of traced rays is required, as it is possible to perturb a model while keeping the RMS and χ^2value within an acceptable range if the number of traced rays is significantly reduced.

The parameter uncertainty is thus the maximum perturbation that causes the inverted model to exceed any of the thresholds. These threshold values are plotted along with acceptance and rejection bands (Figure 7), which helps to interpret global trends and to identify minima of RMS and χ^2. Normally, not all thresholds are exceeded for the same perturbation size. A specific threshold, or even all four, may never be reached, due to poor constraint, reduced ray coverage, smearing, or other causes. In this case, it is assumed to be indeterminable by this method. Error bounds are generally asymmetrical and equally well resolved parameters may have different error bounds due to smearing.

When compared to the single parameter uncertainty estimation proposed by Zelt (1999), VMONTECARLO provides an evaluation of the uncertainties of all parameters of interest simultaneously, taking into account smearing and other parameter interdependencies, also giving further information about the expected reliability of these uncertainties, and providing additional insights on the quality of models as it highlights local minima and alternative solutions.

5.3. Comparison with Clark et al. (2013)

Another method to estimate model uncertainty via Monte Carlo simulations has been proposed by Clark et al. (2013), based on the work of Mosegaard & Tarantola (1995) as implemented by Hauser et al. (2011). In some aspects, VMONTECARLO is similar to this method, as both test a given parametrisation by generating perturbed models with Monte Carlo simulations, and both provide estimations of uncertainty, but they take different approaches to the problem.

The method proposed by Clark et al. (2013), explores the model space defined by a given parametrisation and some velocity bounds in search of a model with a good fit without operator intervention, apart from the choice of parametrisation. This method finds a model by semi-automatic means and uncertainty estimates are obtained by statistical analysis of the parameters in the accepted simulations.

On the other hand, VMONTECARLO provides alternate solutions when evaluating the uncertainty of a preferred model, by exploring the solution space around it for models of similar or better fit. The model acceptance criteria can be made more or less strict by means of a shape factor in the scoring function, and the uncertainty estimates are calculated from a minimum definable relative model quality, with regard to the preferred model's quality, i.e, the user defines how much worse than the preferred model can a random model be before being rejected. Bad models are not completely rejected, as they are used to build score dispersion maps for further interpretation. In VMONTECARLO, all the random models are generated by independently perturbing all the parameters of interest of the preferred model. In the method proposed by Clark et al. (2013), each new model is obtained by the perturbation of a single parameter of the previous iteration that was accepted into the set of posterior distribution samples.

VMONTECARLO runs considerably faster when compared to the method of Clark et al. (2013), where 100 000 iterations on the PETROBAR-07 profile took 88 hours to run on four threads of the TITAN III cluster. The same number of iterations took, writing data to disk on a single thread of a standard desktop computer, a little over 9 hours for a 250 km excerpt of profile SB02. The main performance bottleneck is disk access, as a similar run using only RAM, took a little over 2.5 hours for the same model. Another advantage of VMONTECARLO is the seamless integration with typical

RAYINVR modelling strategies, using the unchanged data and configuration files at any modelling stage.

Consecutive runs to increase the number of simulations for a given model are directly handled by VMONTECARLO, building upon previous results. Concurrent execution is also possible (and desirable), with a final results-merging step needed.

VMONTECARLO has the advantage of providing detailed histograms (Figure 16) of the studied parameter values for all models within a pre-defined quality band. This extra information sheds light not only on the maximum and minimum bounds for the parameter value, but also their trends.

Both methods share some limitations:*a*) the uncertainties estimation builds upon the effective sampling of the solution space, but with a larger number of simulations we can increase the robustness of the results; *b*) layer modelling is extremely dependent on the choices of the operator in terms of picking and identifying seismic phases, and establishing the minimum structure capable of justifying the data. Proper phase to interface identification must be assumed on both methods; *c*) and the assumption that parameter values are normally distributed. If they are not, different statistical tools are needed.

VMONTECARLO does not smooth lateral velocity gradients or interface topographies, nor does it explicitly avoid velocity inversions. Low-velocity layers are difficult to model because they can hide or distort arrivals and have a non-dismissible effect on travel times, but, because all parameters are randomly varied at the same time, it is expected that, for a sufficiently large number of simulations, the solution space is adequately sampled with good and bad models. If models with sharp or unrealistic contrasts are created, they will most likely perform poorly in the ray-tracer.

6. Conclusions

Travel time inversion and forward modelling techniques have limitations in terms of resolution and uncertainties and most of these limitations are shared with parametrisations as they arise from the capabilities of the imaging systems. Velocity model interpretation cannot be confined to the plotted interface depths and velocities, and parameter uncertainties are an integral part of the results, as alternate solutions within the expected error margin must also be taken into account. Model evaluation, in terms of quality, reliability and associated uncertainty is paramount for a good understanding of the structures the model represents. A complete model evaluation must include a measure of the confidence on the model.

VMONTECARLO gives added confidence to geological interpretations as it limits model uncertainty, and even in cases where uncertainties are large, it is capable of distinguishing structures with

different lithological signatures. If used to sound the solution space, VMONTECARLO escapes eventual numerical problems in an unbiased way because it is not sensitive to local minima that may trap the inversion algorithms if the model to invert is not already close to the solution (Zelt & Smith, 1992). Additionally, with a sufficiently large ME, it provides an estimate of the probability distribution of parameter values.

There are other stochastic methods to build and evaluate layered velocity models available (Clark et al., 2013) that also provide uncertainty estimates, but with different approaches and goals. For the purpose of model uncertainty evaluation, VMONTECARLO is easier to integrate into a normal RAYINVR work-flow.

Models with extremely poor ray coverage or without a sufficient number of identifiable reflected arrivals may have large parameter uncertainties because we cannot adequately constrain the interfaces. Similarly, model parametrization may be too simple to characterize very heterogeneous regions. However, VMONTECARLO can distinguish between models that are well or poorly-constrained by arrival times alone.

A final model might not be the best solution that fits the available data, but a compromise between data, data uncertainty and allowable interface roughness. The preferred model may also take into account subjective operator interpretations based on experience or expectations. Careful model evaluation is needed to avoid potential interpretative bias.

This tool allows to assess model uncertainty at final or intermediate modelling stages, even on those based on forward modelling strategies, avoiding subjective interpretations by generating and scoring random models within the defined the bounds. Further insights into model uncertainty are gained from the distribution of the average scores and parameter histograms.

In the two longer SanBa profiles, SB01 and SB02, the central region appears very different, although they were shot at less than one hundred kilometers apart. There was a need to determine if the lack of reflected arrivals from the Moho in SB01 could bias the geological interpretation. With VMONTECARLO, we have shown that travel times alone are insufficient to model the deep crust on SB01 with uncertainties comparable to those obtained in SB02. In some parts of the studied area, the uncertainty regions of each model overlap (Figure 18a)), or areas where each models uncertainty band do not completely overlap but still admit the other profile's solution (Figure 18c)), meaning that we are unable to categorically affirm that they are different in these areas.

Nevertheless, there are areas where the uncertainties of each model mutually exclude the preferred model of the other profile (Figure 18b)), in which the maximum propagation velocity in the lower crust of SB02 is significantly lower than that of the preferred model of SB01. Although travel times alone admit large uncertainties for SB01, the gradients for the preferred model were constrained

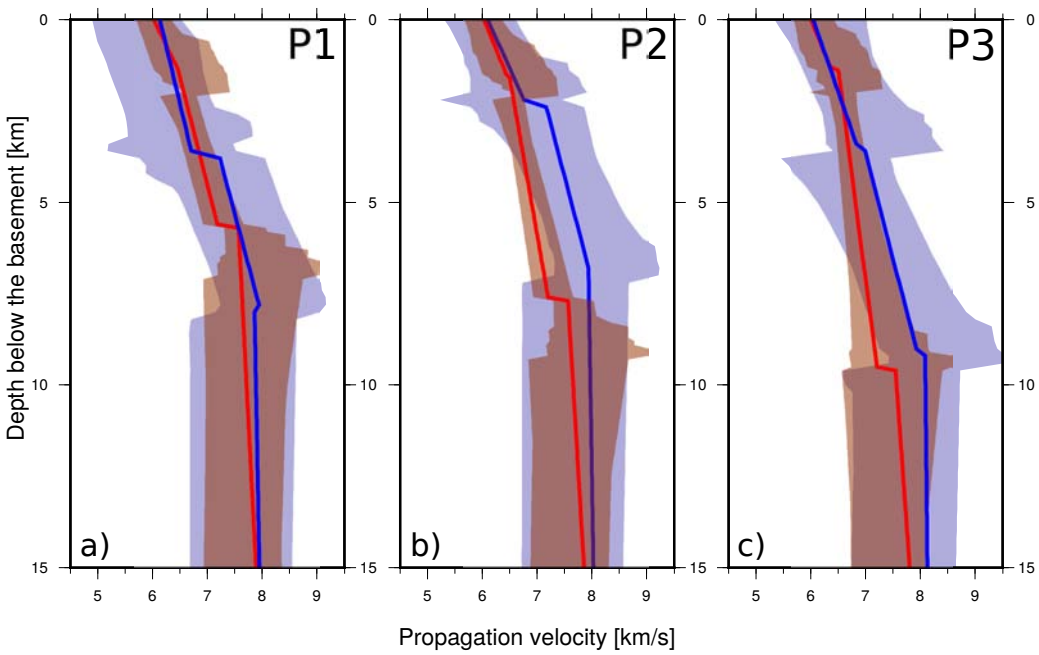

Figure 18: 1D velocity/depth profiles below the basement of the preferred models of SB01 (blue solid lines) and SB02 (red solid lines) at the locations indicated in Figures 1e and 1d, respectively, by black vertical arrows and letters. Blue shaded regions indicate the maximum admissible velocity deviations from the SB01 preferred model. Brown shaded regions indicate maximum admissible velocity deviations from the SB02 preferred model. Profiles P1 and P2 are 20 km apart. Profiles P2 and P3 are 40 km apart.

by amplitude modelling. Also, the lower crust maximum admissible velocities of SB02 are, generally, lower than the preferred model's of SB01 (Figure 18). The structures imaged on both profiles in the area are indeed different. This result highlights the strong heterogeneity of this intermediate area where the rift and probably the first proto-oceanic crust aborted, leaving the entire system of the brazilian side (Evain et al., 2015; Moulin et al., 2012). It supports a relationship between the exhumed lower continental crust and the first proto-oceanic crust as suggested by Aslanian et al. (2009) following Bott (1971). These lateral variations show the necessity to design wide-angle experiments with close parallel and also crossing profiles.

7. Acknowledgments

We thank Philippe Schnurle for sharing his valuable insights. We also thank Matthias Delescluse, Louise Watremez, and an anonymous reviewer for their excellent suggestions, and their constructive and exhaustive reviews that significantly improved this manuscript.

The GMT (Wessel & Smith, 1998) software package was extensively used in the preparation of this paper

This study is co-funded by Ifremer, IDL, IUEM, UnB and Petrobras as part of the MAGIC scientific project. The Ph.D. Thesis of Afonso Loureiro is also supported by an IDL grant co-financed by FFCUL.

8. Contributions

The SanBa Project was led by D. Aslanian and M. Moulin, from Ifremer, A. Loureiro developed VMONTECARLO, with supervision from A. Afilhado, L. Matias and M. Moulin. Modelling of the SanBa profiles was done by M. Evain, A. Afilhado, C. Rigotti, A. Loureiro, D. Alves, F. Klingelhöfer and A. Feld. This work was done on a original idea of D. Aslanian.

9. References

A. Afilhado, L. Matias, H. Shiobara, A. Hirn, L. Mendes-Victor, and H. Shimamura. From unthinned continent to ocean: the deep structure of the West Iberia passive continental margin at 38 N. *Tectonophysics*, 458(1):9–50, 2008. doi: 10.1016/J-TECTO.2008.03.002.

D. Aslanian and M. Moulin. Palaeogeographic consequences of conservational models in the South Atlantic Ocean. *Geological Society, London, Special Publications*, 369(1):75–90, 2012. doi: 10.1144/SP369.5.

D. Aslanian, M. Moulin, J.-L. Olivet, P. Unternehr, L. Matias, F. Bache, M. Rabineau, H. Nouzé, F. Klingelhöfer, I. Contrucci, et al. Brazilian and African passive margins of the Central Segment of the South Atlantic Ocean: Kinematic constraints. *Tectonophysics*, 468(1):98–112, 2009. doi: 10.1016/J.TECTO.2008.12.016.

M. Bott. Evolution of young continental margins and formation of shelf basins. *Tectonophysics*, 11 (5):319–327, 1971. doi: 10.1016/0040-1951(71)90024-2.

J. E. Bresenham. Algorithm for computer control of a digital plotter. *IBM Systems journal*, 4(1): 25–30, 1965. doi: 10.1147/SJ.41.0025.

V. Cervený, I. Molotkov, and I. Psencik. *Ray method in seismology*. Univerzita Karlova, 1977.

N. Christensen and W. Mooney. Seismic velocity structure and composition of the continental crust: A global view. *Journal of Geophysical Research Atmospheres*, (100):9761–9788, 1995. doi: 10.1029/95JB00259.

S. A. Clark, J. I. Faleide, J. Hauser, O. Ritzmann, R. Mjelde, J. Ebbing, H. Thybo, and E. Flüh. Stochastic velocity inversion of seismic reflection/refraction traveltime data for rift structure of the southwest Barents Sea. *Tectonophysics*, 593:135–150, 2013. doi: 10.1016/J.TECTO.2013.02.033.

C. Croarkin and P. Tobias. *NIST/SEMATECH e-Handbook of Statistical Methods*. NIST/SEMATECH. Available online: http://www. itl. nist. gov/div898/handbook, 2012. Last access: 2016-03-21.

M. Delescluse, T. Funck, S. A. Dehler, K. E. Louden, and L. Watremez. The oceanic crustal structure at the extinct, slow to ultra-slow Labrador Sea spreading center. *Journal of Geophysical Research: Solid Earth*, 2015. ISSN 2169-9356. doi: 10.1002/2014JB011739.

J. D. Eccles, R. S. White, and P. A. Christie. Identification and inversion of converted shear waves: case studies from the European North Atlantic continental margins. *Geophysical Journal International*, 179(1):381–400, 2009. doi: 10.1111/j.1365-246X.2009.04290.x.

M. Evain, A. Afilhado, C. Rigoti, A. Loureiro, D. Alves, F. Klingelhöfer, P. Schnurle, A. Feld, R. Fuck, J. Soares, M. Vinicius de Lima, C. Corela, L. Matias, M. Benabdellouahed, A. Baltzer, M. Rabineau, A. Viana, M. Moulin, and D. Aslanian. Deep structure of the Santos Basin-São Paulo Plateau System, SE Brazil. *Journal of Geophysical Research*, 2015.

L. A. Gallardo and M. A. Meju. Structure-coupled multiphysics imaging in geophysical sciences. *Reviews of Geophysics*, 49(1), 2011. ISSN 1944-9208. doi: 10.1029/2010RG000330.

J. Hauser, K. M. Dyer, M. E. Pasyanos, H. Bungum, J. I. Faleide, S. A. Clark, and J. Schweitzer. A probabilistic seismic model for the European Arctic. *Journal of Geophysical Research: Solid Earth (1978–2012)*, 116(B1), 2011. doi: 10.1029/2010JB007889.

W. S. Holbrook, E. Reiter, G. Purdy, D. Sawyer, P. Stoffa, J. Austin, J. Oh, and J. Makris. Deep structure of the US Atlantic continental margin, offshore South Carolina, from coincident ocean bottom and multichannel seismic data. *Journal of Geophysical Research: Solid Earth (1978–2012)*, 99(B5):9155–9178, 1994. doi: 10.1029/93JB01821.

W. S. Holbrook, T. M. Brocher, U. S. ten Brink, and J. A. Hole. Crustal structure of a transform plate boundary: San Francisco Bay and the central California continental margin. *Journal of Geophysical Research: Solid Earth (1978–2012)*, 101(B10):22311–22334, 1996. doi: 10.1029/96JB01642.

D. D. Jackson. Interpretation of Inaccurate, Insufficient and Inconsistent Data. *Geophysical Journal International*, 28(2):97–109, 1972. doi: 10.1111/j.1365-246X.1972.tb06115.x.

V. Karastathis, S. Papamarinopoulos, and R. Jones. 2-D velocity structure of the buried ancient canal of Xerxes: an application of seismic methods in archaeology. *Journal of Applied Geophysics*, 47 (1):29 – 43, 2001. ISSN 0926-9851. doi: 10.1016/S0926-9851(01)00045-3.

F. Klingelhöfer, M. Evain, A. Afilhado, C. Rigoti, A. Loureiro, D. Alves, A. Leprêtre, M. Moulin, P. Schnurle, M. Benabdellouahed, A. Baltzer, M. Rabineau, A. Feld, A. Viana, and D. Aslanian.

Imaging proto-oceanic crust off the Brazilian Continental Margin. *Geophysical Journal International*, 2014. doi: 10.1093/GJI/GGU387.

V. T. Leinweber, F. Klingelhöfer, S. Neben, C. Reichert, D. Aslanian, L. Matias, I. Heyde, B. Schreckenberger, and W. Jokat. The crustal structure of the Central Mozambique continental margin – Wide-angle seismic, gravity and magnetic study in the Mozambique Channel, Eastern Africa. *Tectonophysics*, 599:170–196, 2013. doi: 10.1016/J.TECTO.2013.04.015.

M. Majdański. The uncertainty in layered models from wide-angle seismic data. *Geophysics*, 78(3): WB31–WB36, 2013. doi: 10.1190/GEO2012-0280.1.

M. McCaughey and S. C. Singh. Simultaneous velocity and interface tomography of normal-incidence and wide-aperture seismic traveltime data. *Geophysical Journal International*, 131(1): 87–99, 1997. doi: 10.1111/J.1365-246X.1997.TB00596.X.

K. Mosegaard and A. Tarantola. Monte Carlo sampling of solutions to inverse problems. *Journal of Geophysical Research: Solid Earth (1978–2012)*, 100(B7):12431–12447, 1995. doi: 10.1029/94JB03097.

M. Moulin, D. Aslanian, and P. Unternehr. A new starting point for the South and Equatorial Atlantic Ocean. *Earth-Science Reviews*, 98(1):1–37, 2010. doi: 10.1016/j.earscirev.2009.08.001.

M. Moulin, D. Aslanian, M. Rabineau, M. Patriat, and L. Matias. Kinematic keys of the Santos–Namibe basins. *Geological Society, London, Special Publications*, 369(1):91–107, 2012. doi: 10.1144/SP369.3.

A. Plaza-Faverola, S. Bünz, and J. Mienert. Fluid distributions inferred from P-wave velocity and reflection seismic amplitude anomalies beneath the Nyegga pockmark field of the mid-Norwegian margin. *Marine and Petroleum Geology*, 27(1):46–60, 2010. doi: 10.1016/J.MARPETGEO.2009.07.007.

F. Press. Earth models obtained by Monte Carlo inversion. *Journal of Geophysical Research*, 73(16): 5223–5234, 1968. doi: 10.1029/JB073I016P05223.

W. H. Press. *Numerical recipes 3rd edition: The art of scientific computing*. Cambridge university press, 2007.

M. Sambridge, K. Gallagher, A. Jackson, and P. Rickwood. Trans-dimensional inverse problems, model comparison and the evidence. *Geophysical Journal International*, 167(2):528–542, 2006. doi: 10.1111/J.1365-246X.2006.03155.X.

D. T. Sandwell, R. D. Müller, W. H. F. Smith, E. Garcia, and R. Francis. New global marine gravity model from CryoSat-2 and Jason-1 reveals buried tectonic structure. *Science*, 346(6205):65–67, 2014. doi: 10.1126/science.1258213.

T. Sato, T. Sato, M. Shinohara, R. Hino, M. Nishino, and T. Kanazawa. P-wave velocity structure of the margin of the southeastern Tsushima Basin in the Japan Sea using ocean bottom seismometers and airguns. *Tectonophysics*, 412(3):159–171, 2006. doi: 10.1016/J.TECTO.2005.09.001.

W. Stratford, H. Thybo, J. I. Faleide, O. Olesen, and A. Tryggvason. New Moho map for onshore southern Norway. *Geophysical Journal International*, 178(3):1755–1765, 2009.

G. F. Viejo and R. M. Clowes. Lithospheric structure beneath the Archaean Slave Province and Proterozoic Wopmay orogen, northwestern Canada, from a Lithoprobe refraction/wide-angle reflection survey. *Geophysical Journal International*, 153(1):1–19, 2003. doi: 10.1046/J.1365-246X.2003.01807.X.

P. Wessel and W. H. Smith. New, improved version of Generic Mapping Tools released. *Eos, Transactions American Geophysical Union*, 79(47):579–579, 1998. doi: 10.1029/98EO00426.

R. S. White, D. McKenzie, and R. K. O'Nions. Oceanic crustal thickness from seismic measurements and rare earth element inversions. *Journal of Geophysical Research: Solid Earth (1978–2012)*, 97 (B13):19683–19715, 1992. doi: 10.1029/92JB01749.

E. P. Wigner. The unreasonable effectiveness of mathematics in the natural sciences. Richard Courant lecture in mathematical sciences delivered at New York University, May 11, 1959. *Communications on pure and applied mathematics*, 13(1):1–14, 1960. doi: 10.1002/cpa.3160130102.

C. A. Zelt. Modelling strategies and model assessment for wide-angle seismic traveltime data. *Geophysical Journal International*, 139(1):183–204, 1999. doi: 10.1046/J.1365-246X.1999.00934.X.

C. A. Zelt and R. M. Ellis. Practical and efficient ray tracing in two-dimensional media for rapid traveltime and amplitude forward modeling. *Canadian Journal of Exploration Geophysics*, 24(1): 16–31, 1988.

C. A. Zelt and R. B. Smith. Seismic traveltime inversion for 2-D crustal velocity structure. *Geophysical Journal International*, 108(1):16–34, 1992. doi: 10.1111/J.1365-246X.1992.TB00836.X.